2020

Quantitative Susceptibility Mapping (QSM) Reconstruction from MRI Phase Data

Sara Gharabaghi
Wright State University

QUANTITATIVE SUSCEPTIBILITY MAPPING (QSM) RECONSTRUCTION

FROM MRI PHASE DATA

A Dissertation submitted in partial fulfillment of the

requirements for the degree of

Doctor of Philosophy

by

SARA GHARABAGHI

M.S., Wright State University, 2018
M.S., Sahand University of Technology, Iran, 2011
B.S., Sahand University of Technology, Iran, 2009

2020

Wright State University

WRIGHT STATE UNIVERSITY

GRADUATE SCHOOL

December 7, 2020

I HEREBY RECOMMEND THAT THE DISSERTATION PREPARED UNDER MY SUPERVISION BY Sara Gharabaghi ENTITLED Quantitative Susceptibility Mapping (QSM) Reconstruction from MRI Phase Data BE ACCEPTED IN PARTIAL FULFILLMENT OF THE REQUIREMENTS FOR THE DEGREE OF Doctor of Philosophy.

_____
E. Mark Haacke, Ph.D.
Dissertation Co-Director

_____
Thomas Wischgoll, Ph.D.
Dissertation Co-Director

_____
Yong Pei, Ph.D.
Director, Computer Science and Engineering Ph.D. Program

_____
Barry Milligan, Ph.D.
Interim Dean of the Graduate School

Committee on Final Examination:

_____
Tanvi Banerjee, Ph.D.

_____
E. Mark Haacke, Ph.D.

_____
Yong Pei, Ph.D.

_____
Thomas Wischgoll, Ph.D.

ABSTRACT

Gharabaghi, Sara. Ph.D., Computer Science and Engineering Department, Wright State University, 2020. Quantitative Susceptibility Mapping (QSM) Reconstruction from MRI Phase Data.

Quantitative susceptibility mapping (QSM) is a powerful technique that reveals changes in the underlying tissue susceptibility distribution. It can be used to measure the concentrations of iron and calcium in the brain both of which are linked with numerous neurodegenerative diseases. However, reconstructing the QSM image from the MRI phase data is an ill-posed inverse problem. Different methods have been proposed to overcome this difficulty. Still, the reconstructed QSM images suffer from streaking artifacts and underestimate the measured susceptibility of deep gray matter, veins, and other high susceptibility regions.

This thesis proposes a structurally constrained Susceptibility Weighted Imaging and Mapping (scSWIM) method to reconstruct QSM for multi-echo, multi-flip angle data collected using strategically acquired gradient echo (STAGE) imaging. scSWIM performs a single step regularization-based reconstruction technique that takes advantage of the unique contrast of the STAGE T1 weighted enhanced (T1WE) image to extract reliable geometry constraints to protect the basal ganglia from over-smoothing. Furthermore, the multi-echo, multi-flip angle data from STAGE can all be used to improve the contrast-to-noise ratio in QSM through a weighted averaging scheme.

scSWIM was tested on both simulated and *in vivo* data. Results show that the unique contrast and tissue boundaries from T1WE and an earlier approach called iterative SWIM enable the accurate definition of the edges of high susceptibility regions. scSWIM achieved the best overall root mean squared error and structural similarity index metrics as well as the lowest deviation from the expected susceptibility in deep gray matter compared to other published methods. Finally, susceptibility measurements of the basal ganglia extracted from the scSWIM data for a cohort of Parkinson's disease patients and healthy control subjects were in agreement with the literature.

TABLE OF CONTENTS

LIST OF FIGURES

LIST OF TABLES

Acknowledgment

I would like to take this opportunity to extend my deepest gratitude to my co-advisor, Dr. E. Mark Haacke. I cannot thank him enough for giving me this opportunity and his invaluable guidance through this research. His profound and thorough knowledge of the fundamentals of MRI Physics has always impressed me, and his perseverance and passion for research are and will always be inspirational sources for me.

I would also like to thank my co-advisor, Dr. Thomas Wischgoll. I cannot even begin to sum up all that I have learned from him, and I am forever thankful for his constant support, believing in me, and helping me find the field that I am most passionate about.

My sincere thanks also go to my dissertation committee Dr. Tanvi Banerjee and Dr. Yong Pei, who graciously agreed to serve on my committee and take their precious time to provide valuable feedback on my research. I would also like to thank Dr. Mateen Rizki, the Computer Science Department chair who always kindly supported me from the beginning of my studies at WSU.

Furthermore, I need to thank my professors, Dr. Arthur A. Goshtasby and Dr. Nasser H. Kashou at Wright State University, who took the time to share their knowledge and deep understanding in medical image processing and analysis and MRI fields. Additionally, I have deep gratitude for Dr. Saifeng Liu and Dr. Sagar Buch, who have

This thesis is dedicated to my wonderful and caring parents and sister,

and

my beloved husband.

1 INTRODUCTION

Magnetic resonance imaging (MRI) is a non-invasive imaging technique that provides useful information about the soft tissues and anatomical structure of the human body. MRI offers many different contrast mechanisms such as T1-weighted and T2-weighted scans. In most of these techniques, the main focus has been using the magnitude information of the acquired complex MRI signal, and the phase information was usually discarded. Almost 20 years after the MRI invention and ignoring the phase, it was discovered that the phase data provides interesting information about the underlying tissue susceptibilities [1] and could be used to detect iron thanks to the resulting changes in the local field [2]. This led researchers to develop new techniques such as Susceptibility Weighted Imaging (SWI) [3] and new reconstruction methods such as Quantitative Susceptibility Mapping (QSM) [4,5].

SWI [3] is a technique that incorporates the gradient echo imaging (GRE) phase information to generate a new contrast based on the magnetic susceptibility of the tissues. SWI combines the magnitude and filtered phase [6,7] to enhance the visualization of the tissues with high iron content and venous blood vessels (thanks to the presence of deoxyhemoglobin in the blood). Although SWI provides unique information about the underlying tissues, it is qualitative in nature and cannot quantitatively assess the amount of iron deposited in the tissue.

The need for quantitative information that allows assessing the susceptibility of the underlying tissues led to the development of QSM. Similar to the SWI phase mask used to enhance the contrast, QSM data are reconstructed from the phase information of the GRE data (since phase is directly proportional to the magnetic field variations caused by the magnetization of an object in the presence of an external magnetic field [8]). The resulting susceptibility maps can be used to assess bleeding [9], calcium deposits [3,4], demyelination, and oxygen saturation [12]. The knowledge of the susceptibility source and the quantity of either iron or calcium can help improve the diagnosis of neurodegenerative diseases [8] such as multiple sclerosis [13], Parkinson's disease [7,8], Huntington disease [16], stroke [17], Sturge-Weber syndrome [18], and traumatic brain injury [19].

Reconstructing the susceptibility from GRE phase data is an ill-posed problem because the dipole kernel has zeroes along a conical surface and, therefore, under-samples k-space [8]. Many studies have attempted to solve this problem using single and multiple orientation MRI data [13–18]. However, the susceptibility values in the reconstructed QSM images are underestimated and streaking artifacts emanate from regions with high susceptibility. Furthermore, most of these methods find the total field through a linear fitting of multi-echo phase data. Therefore, the inclusion of long echo times in these methods can lead to blooming artifacts, an increase in the signal loss at the edges of the object and, potentially, an underestimation of χ.

A few years ago, Strategically Acquired Gradient Echo (STAGE) imaging was introduced to the field [26–28]. STAGE is currently being tested on a variety of scanners (at field strengths of 0.35T up to 7T) at over fifty sites worldwide for a number of neurodegenerative diseases [28]. STAGE is a multi-contrast multi-parametric imaging approach that employs two fully-flow compensated, double-echo, GRE scans using low and high flip angles.

STAGE provides not only a variety of qualitative images such as the T1 weighted enhanced (T1WE) image, but also provides multiple quantitative information such as R_2^*, T1, and single-echo susceptibility maps [26–28]. The improved contrast in the T1WE image between cortical grey matter and white matter, and between deep grey matter and white matter [27] provides an opportunity to derive accurate structural information about the underlying tissues. Furthermore, having multi-echo, multi-flip angle scans, STAGE has the potential to provide improved contrast-to-noise through a weighted averaging of the single echo QSM data.

Therefore, in this study, we have focused on developing the scSWIM method as a means to reconstruct the susceptibility map using multi-echo and multiple flip angle STAGE data. scSWIM utilizes the structural information from both magnitude data and the susceptibility maps themselves in a single step. The proposed method was tested on simulated data and *in vivo* human brain data from healthy controls and patients.

1.1 Contributions

In this study, we propose the scSWIM method as a single step ℓ_1- and ℓ_2-norm based regularization method to reconstruct QSM from MRI phase data. This approach specifically takes advantage of the enhanced contrast available in STAGE imaging to define prior information about the edges of the white matter, gray matter, and deep gray matter structures. It also uses iSWIM as an initial susceptibility map to extract the structural information about the veins, deep gray matter structures, and other high susceptibility structures. Having accurate information about the underlying tissue is crucial in recovering the missing information in k-space and reducing streaking artifacts.

Furthermore, scSWIM has been adapted to use multi-parametric STAGE scans to generate the final integrated multi-echo, multi-flip angle scSWIM. This is performed by a cascade framework to get the scSWIM data for each echo as they are used as the initial guess for the next echo. Then, an R_2^*-based weighted averaging of these individual echo scSWIMs is used to get the final STAGE scSWIM which has improved signal-to-noise. Additionally, it helps to avoid blooming artifacts and underestimation of the susceptibility map that happens in other methods which are due to the inclusion of the longer echo in the linear fitting of the multi-echo phase process to get the field map. Furthermore, the loss of tissues associated with the use of a phase quality control map (especially at longer echo times) will be, to a large degree, replaced with the shorter echo scSWIM value.

4

1.2 Outline of the Thesis

The outlines of this thesis is as follows: Chapter 2 starts by introducing the concept of GRE imaging and the STAGE imaging protocol. Then, the magnetic susceptibility and the problem of reconstructing QSM as an inverse problem are explained. At the end of this chapter, the required phase preprocessing steps and QSM reconstruction methods proposed in the literature are reviewed. In Chapter 3, the proposed method, scSWIM, is discussed for both single-echo data and multi-echo STAGE data. In this chapter, the simulated and *in vivo* test data used to evaluate the scSWIM are also described. Results are discussed in Chapter 4. In Chapter 5, the structural constraints of scSWIM, the selection of its parameters, and the use of STAGE imaging in scSWIM are discussed. Most of the contents of Chapters 3, 4 and 5 have been directly adapted or expanded from our published conference paper [29] and journal paper [30]. Finally, the conclusion and future directions of this research project are presented in Chapter 6.

2 BACKGROUND

2.1 Gradient Recalled Echo (GRE) Imaging

GRE imaging does not use a spin echo (SE) refocusing pulse thereby providing lower specific absorption rate imaging and the potential for faster imaging since repeat times (TR) can be significantly shortened. When short TRs are used, the signal can be maximized by choosing the flip angle equal to the Ernst angle. The choice of flip angle much less than the Ernst angle generates a spin density weighted image while a flip angle larger than the Ernst angle generates a T1W image. The GRE sequence also provides T2*-contrast when the echo time is on the order of the T2* of the tissue. These varies imaging parameter changes opens the door to generating new contrasts and interesting diagnostic information.

Based on the physics of MRI [31], when the body is positioned in the scanner, the randomly oriented hydrogen protons align their spins tend to align more along the direction of the external magnetic field, B_0. In this state, a torque is applied on the spins that causes the protons to precess or wobble around B_0. The precession angular frequency, ω_0, is called the Larmor frequency and depends on the strength of B_0:

$$\omega_0 = \gamma B_0, \tag{2.1}$$

where $\gamma = 2.675 \times 10^8 \ rad/s/T$ is the gyromagnetic ratio for hydrogen protons. In the next step, a Radio Frequency (RF) field is turned on orthogonal to the B_0 direction. Viewed in the rotating reference frame, this second (oscillating) magnetic field causes the spins to

precess toward the plane transverse to the main field. The frequency of this RF pulse is set equal to the frequency of the protons in the excited slice. If a gradient is applied along the slice direction, by setting a certain bandwidth to the RF pulse, a slice of spins can be modified (this is referred to as slice selection). Since the RF field is perpendicular to B_0, the net magnetization vector rotates away from M_0 in the z-direction onto the xy plane. The amount of rotation that M_0 experiences during the application of the RF pulse over a certain time duration is called the Flip Angle (FA). At this stage, the net magnetization has two components of longitudinal M_z, (parallel to) and transverse M_{xy}, orthogonal to B_0.

Both frequency and phase encoding gradients can be applied after the slice excitation to create spatial information about the spins that is extracted as an image in 2 dimensions (2D) . Once the RF pulse is turned off, protons tend to relax back to their resting state leading to a recovery of the longitudinal magnetization toward its equilibrium value. This recovery rate depends on the intrinsic T_1-relaxation time (spin-lattice relaxation) of the tissue as follows:

$$M_z(t) = M_0(1 - e^{-t/T_1}).$$
(2.2)

On the other hand, when there are no macroscopic gradients present, the transverse magnetization decays exponentially depending on the T2 relaxation time (spin-spin relaxation):

$$M_{xy}(t) = M_0 e^{-t/T_2}.$$
(2.3)

However, in the presence of macroscopic gradients, as occurs in GRE imaging, M_{xy} decays faster than T₂ due to the subsequent spin dephasing via T2* (where $T_2^* \leq T_2$) via:

$$\frac{1}{T_2^*} = \frac{1}{T_2} + \frac{1}{T_2'} \,. \tag{2.4}$$

The precessing transverse magnetization induces a voltage V in the receiver coils (which are placed perpendicular to the transverse plane) according to:

$$V(t) = \kappa M_0 e^{i\omega_0 t} e^{-t/T_2}, \tag{2.5}$$

where κ is constant. Since this voltage appears as damped oscillating function, it is referred to as the Free Induction Decay (FID). The detected signal is then demodulated, digitized and then sent to a computer to be processed for the reconstruction of the MRI image.

Figure 2.1 illustrates the GRE pulse sequence. It includes a single RF excitation pulse, usually with a FA lower than 90°. A gradient, $G_{z,SS}$, is turned on during the RF pulse to allow for slice excitation, however, this gradient also leads to dephasing in the slice selection direction. Therefore, a rephasing gradient is used just after the slice selection gradient to correct this issue. Immediately afterward, a phase encoding gradient, $G_{y,PE}$, is applied in the y-direction and usually the dephasing lobe of the frequency encoding gradient is applied at the same time. Next, the frequency encoding gradient, $G_{x,R}$, is applied in the x-direction. Right after the RF pulse is turned off, the transverse magnetization that was created begins to decay as described above leading to a T_2^* related signal loss. The dephasing lobe causes a rapid dephasing of the protons and to create a gradient echo, the

gradient is reversed, and the protons are rephased at the echo time *TE*. The data are sampled about this time for a duration of Ts as shown in Figure 2.1.

The magnitude signal intensity for a voxel in GRE imaging using a flip angle of θ, an echo time TE and a repeat time TR is given by the Ernst equation [31]:

$$\rho(\theta, TE) = \rho_0 \sin\theta \, \frac{1 - e^{-TR/T1}}{1 - \cos\theta \, e^{-TR/T1}} e^{-TE/T_2^*}, \qquad (2.6)$$

where ρ_0 is the tissue proton density. This signal can be maximized for any given tissue using an
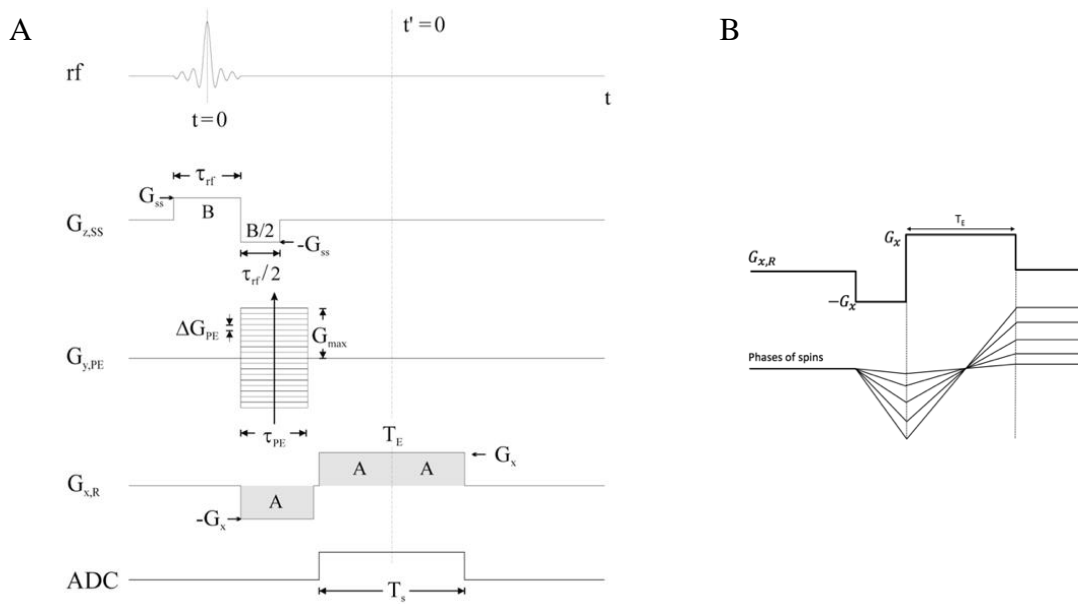
Figure 2.1. Gradient echo sequence (A), and proton spin created by gradient echo (B) (adapted from [31]).

optimal flip angle, θ_E, that is called Ernst angle and is given by $\theta_E = \cos^{-1}(e^{-\frac{TR}{T1}})$. The phase component of the GRE signal is discussed in Section 2.4.

2.2 STAGE Imaging

STrategically Acquired Gradient Echo Iimaging (STAGE) [12–14] is a rapid multi-contrast multi-parametric imaging approach that employs two fully-flow compensated double-echo GRE scans using low and high FAs relative to the Ernst angle of white matter ($\theta_{E,WM} = 15°$ for TR=20ms). These FAs are chosen as 6° and 24° to produce proton density-weighted and T1-weighted scans, respectively.

Figure 2.2 shows the STAGE data processing workflow. STAGE provides not only a variety of qualitative images such as the T1 weighted enhanced (T1WE) image, but also provides multiple quantitative information such as R_2^*, T1, and susceptibility maps [12–14]. The T1WE image is generated from the combination of two GRE scans with low and high FAs [26] where the RF transmit field variation is effectively corrected [27]. When compared with conventional T1W or T2*W images, the T1WE images derived from STAGE have improved contrast between cortical grey matter and white matter, and between deep grey matter and white matter. The improved contrast in the T1WE image can benefit structural segmentation methods.
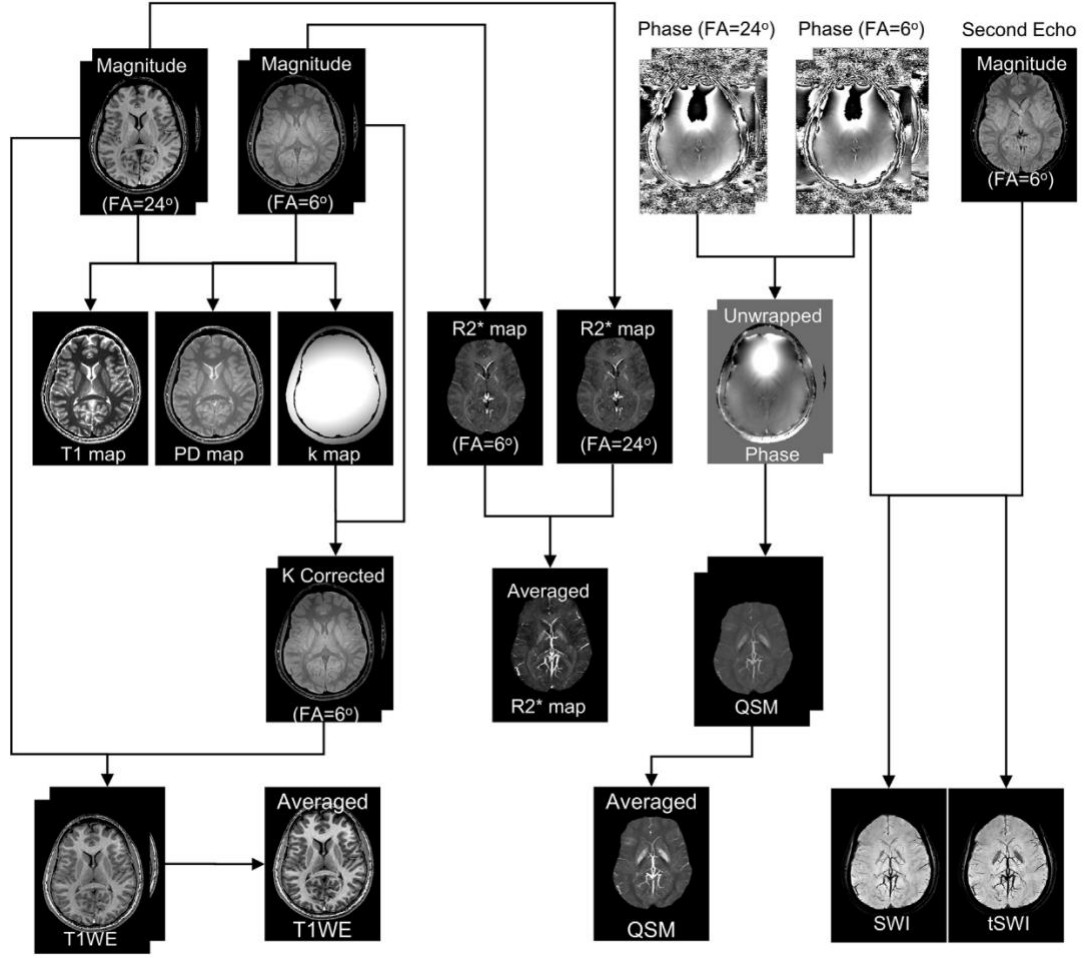
Figure 2.2. STAGE data processing workflow. This figure is adopted from [26].

Another aspect of STAGE is the multi-flip angle R_2^* $(1/T_2^*)$ map that is created from averaging the R_2^* maps from each of the double-echo low and high flip angle scans [19,20]. Each individual R_2^* map is generated from the following formula:

$$R_2^* = \frac{1}{TE_1 - TE_2} ln\left(\frac{\rho_2}{\rho_1}\right), \tag{2.7}$$

where ρ_1 and ρ_2 are the magnitudes of the first (TE_1) and second (TE_2) echoes of the double-echo scan, respectively.

2.3 Magnetic Susceptibility

Magnetic susceptibility, χ, is the physical property of a substance that measures the magnetization of the substance in the presence of an external magnetic field. It is a dimensionless quantity and is usually stated in terms of parts per million (ppm) or parts per billion (ppb). The susceptibility difference of underlying tissues is the main source of magnetic field variation and will be evident predominantly in phase images but can also manifest dephasing effects in the magnitude images [31].

Materials can be classified into three groups based on their magnetic susceptibility properties. The first group is called paramagnetic in which an unpaired electron is present in their atoms. The atoms of paramagnetic material have permanent magnetic moments that are distributed randomly. However, in the presence of an external magnetic field, these small magnets are aligned themselves parallel to the external magnetic field. Paramagnetic materials have positive susceptibility. Deoxyhemoglobin, ferritin and hemosiderin are all examples of paramagnetic materials in human beings.

The second group is called diamagnetic material. The atoms of diamagnetic substances have paired electrons; therefore, they resist aligning parallel to the external

magnetic field. The susceptibility of diamagnetic substances, such as calcium, are negative. Myelin that is composed of lipids and proteins found in abundance in the human brain white matter is diamagnetic relative to demyelinated white matter.

The third group is ferromagnetic materials. The magnetic properties of these materials are somehow similar to the paramagnetics. However, unlike paramagnetic material, the induced magnetic moment from the external magnetic field is permanent in the Ferromagntics and remains even after turning off the external field [31]. Ferric oxide, iron particulates, and gadolinium are examples of ferromagnetic materials. These materials are usually used as contrast agents since they generate large local fields and signal loss where they are deposited. Although the iron is ferromagnetic, it is stored in the form of ferritin and hemosiderin in the human body that both are paramagnetic [32].

2.4   Quantitative Susceptibility Mapping as an Inverse Problem

The phase of the 3D GRE imaging data, $\varphi(\vec{r})$, can be written as:

$$\varphi(\vec{r}) = \gamma\, B_0\, TE\, \delta B(\vec{r}), \tag{2.8}$$

where $\vec{r}$, B_o and TE are the voxel position vector in the image domain, the main magnetic field strength (in Tesla), and the echo time, respectively; $\gamma = 2.675 \times 10^8\ rad/s/T$ is the

gyromagnetic ratio; and $\delta B(\vec{r})$ denotes the normalized local field relative to neighboring tissues.

Based on Maxwell's equations, the relationship between the local field (extracted from the phase of the 3D GRE data), $\delta B(\vec{r})$, and the underlying susceptibility, $\chi(\vec{r})$, in ppm (parts per million) is formulated as [33]:

$$\delta B(\vec{r}) = d(\vec{r}) * \chi(\vec{r}), \tag{2.9}$$

where $*$ denotes the convolution operator between $\chi(\vec{r})$ and the unit dipole kernel $d(\vec{r})$:

$$d(\vec{r}) = \frac{3\cos^2\theta - 1}{4\pi r^3}, \tag{2.10}$$

and θ is the angle between $\vec{r}$ and the direction of the magnetic field B_o. Figure 2.3.A shows the surface of the dipole kernel $d(\vec{r})$.

Using the properties of the Fourier transform, the convolution operation in image space can be written as the voxel-wise multiplication in the frequency domain (k-space):

$$\delta B(\vec{r}) = F^{-1}\left\{D(\vec{k})F\{\chi(\vec{r})\}\right\}, \tag{2.11}$$

where F and F^{-1} denote the Fourier and inverse Fourier transform operators, respectively.
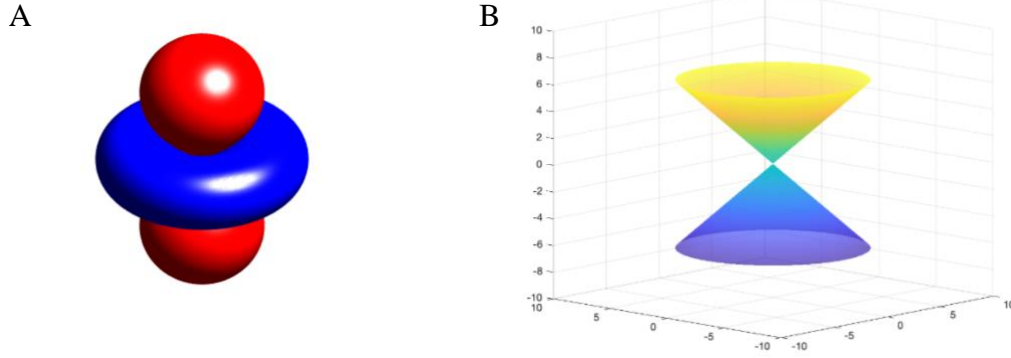
Figure 2.3. Dipole surface rendered contour in spatial space (A), and Dipole zeros in k-space (frequency domain) (B).

Additionally, $D(\vec{k})$ is the Fourier transform of the unit dipole kernel, $d(\vec{r})$, at the position $\vec{k} = [k_x, k_y, k_z]$ in k-space and is defined as:

$$D(\vec{k}) = \frac{k_x^2 + k_y^2 - 2k_z^2}{3\left(k_x^2 + k_y^2 + k_z^2\right)} = \frac{1}{3} - \frac{k_z^2}{|k|^2}. \tag{2.12}$$

The dipole function in k-space has zero values on the double cone surface that makes a 54.7° angle with the direction of the main magnetic field (z-axis). Figure 2.3.B shows the zeros of $D(\vec{k})$ in k-space. Therefore, the inverse problem of reconstructing $\chi(\vec{r})$ from the GRE pre-processed phase information (local field), $\delta B(\vec{r})$, is an ill-posed problem:

$$\chi(\vec{r}) = F^{-1}\left\{D^{-1}(\vec{k})\, F\{\delta B(\vec{r})\}\right\}. \tag{2.13}$$

Note that since $\delta B(\vec{r})$ is a relative value, the reconstructed susceptibility map, $\chi(\vec{r})$, is not an absolute quantity but also a relative measure.

2.5   Data Preprocessing

The QSM reconstruction pipeline generally includes three steps: extracting the region of interest (the brain in this study), unwrapping the acquired phase, and background field removal. In the following sections, we will discuss each of these steps in more detail.

2.5.1   Brain Extraction

Brain extraction is used to separate the brain from the outside zero signal background region. This separation is later needed in the background field removal step. The Brain Extraction Tool (BET) [34] is an automated method for segmenting the brain in T1 and T2 weighted images. BET uses a deformable surface model to find the best segmentation of the brain and non-brain regions. It uses a surface growing algorithm with a locally adaptive growth factor to achieve a smooth surface. BET is fast and freely available as a standalone program.

2.5.2   Phase Unwrapping

The phase data that is obtained from the GRE complex signal is limited to the finite range of $[-\pi, \pi)$. However, the field variations can lead to true phase values that lie outside this range. When the true phase exceeds π, then the phase aliases or wraps back to $-\pi$. These phase jumps appear as what are referred to as zebra stripes in MRI. Therefore, to recover

the true phase, a phase unwrapping step is needed to unwrap the data. Assuming the true unwrapped phase is $\varphi(\vec{r})$, then in terms of the wrapped phase, $\varphi_W(\vec{r})$, at voxel $\vec{r}$, we have:

$$\varphi(\vec{r}) = \varphi_W(\vec{r}) + 2\pi\, n(\vec{r}), \tag{2.14}$$

where $n(\vec{r})$ is an integer. The goal of unwrapping methods is to estimate $n(\vec{r})$ for every voxel, and consequently, the unwrapped phase $\varphi(\vec{r})$. A variety of different methods have been proposed to tackle this problem [35–38]. They can be grouped into single-echo phase unwrapping [35,36], and multi-echo phase unwrapping categories [37,38].

In the single-echo phase unwrapping category, Laplacian phase unwrapping [35] is one of the most commonly used methods. It uses Laplacian operators to get the $n(\vec{r})$:

$$n(\vec{r}) = \frac{1}{2\pi} \nabla^{-1} \big[\nabla \varphi(\vec{r}) - \nabla \varphi_W(\vec{r}) \big], \tag{2.15}$$

where ∇ and ∇^{-1} are denoting the forward and inverse Laplacian operators. In [35], this equation is solved in the frequency domain using the Fourier transform and then the true values of the unwrapped phase are estimated. The performance of Laplacian phase unwrapping is reduced in the regions with high phase gradients such as at the edge of the brain or at air-tissue interfaces where the lack of spatial continuity of phase occurs.

Another frequently used single-echo unwrapping approach is the 3D quality-guided phase unwrapping [36]. This method is based on a quality map that is extracted from the data and represents the phase information reliability of each voxel. Then the unwrapping

starts from the most reliable voxel and ends at the least reliable voxel. The unwrapping process follows a discreet path that prevents the propagation of the error.

On the other hand, multi-echo approaches are presented to address the phase unwrapping problem taking advantage of the evolution of the phase in each voxel through different echoes. One of the methods in this category is the Catalytic Multi-echo Phase Unwrapping Scheme (CAMPUS) [37]. CAMPUS is proposed for multi-echo MRI data with short inter-echo spacing where the first echo is flow compensated and is used as a reference. This method assumes that the phase evolution between two adjacent echoes at each voxel is always less than $\pm\pi$. Unlike the Laplacian phase unwrapping method, CAMPUS is able to correctly unwrap the phase in the regions with higher gradients.

Another similar method for multi-echo data is proposed by Chen et al. [38]. This method is based on acquiring a 2.5ms dataset, along with generating a short pseudo-echo dataset by complex dividing the two phase datasets with short echo spacing (ΔTE) and then unwrapping other echoes using a bootstrapping approach. As mentioned in Equation (2.8), the phase data of GRE imaging at the ith echo time is proportional to the TE_i. Therefore, the unwrapped phase using the bootstrapping approach is obtained by:

$$\varphi_{\text{UW}}(\text{TE}_i, \vec{r}) = \varphi(\text{TE}_i, \vec{r}) - 2\pi \cdot \left[\frac{\varphi(\text{TE}_i, \vec{r}) - (\frac{TE_i}{TE_{i-1}} \cdot \varphi_{\text{UW}}(\text{TE}_{i-1}, \vec{r}))}{2\pi}\right], \tag{2.16}$$

18

where [ ] denotes the rounding operator. This method is compared with the Laplacian and guided 3DSRNCP and reported to be faster and more robust. The limitation of this work is that it relies on the complex divided short pseudo-echo phase data to be unaliased in the entire brain region.

Please note that for the rest of this thesis, we will drop the dependence on $\vec{r}$ for convenience.

2.5.3 Background Field Removal

The last step of phase preprocessing for the QSM reconstruction is to generate the local field, ΔB_L (where $\Delta B_L = B_0 \delta B$), by removing the induced field from the background around the brain as the object of interest. The field variation, ΔB, in Equation (2.8), can be formulated as:

$$\Delta B = \Delta B_L + \Delta B_B, \tag{2.17}$$

where ΔB_L and ΔB_B are denoting the local and background fields. The source of the induced background field is mainly from the air-tissue interfaces (sinuses in the head) and magnetic field inhomogeneities.

Different methods have been proposed to address the background field removal problem. The homodyne high-pass filtering is one of the most used methods in the literature such as used in the well-known Susceptibility Weighted Imaging (SWI) approach [3].

Homodyne high-pass filtering is based on the assumption that the phase changes between different structures of interest have higher frequency. Therefore, a high-pass filter can keep them and remove the background that has lower frequency. In [20–22]. High-pass filtering is used based on the method proposed in [39], where first a low-pass filter is applied to the complex signal in k-space. Then, the signal is complex-divided by the low-pass filtered signal to get the high-pass filtered data, and, consequently, the final phase input to determine the remaining local field. Since this process is applied directly to the complex signal, the result is automatically phase unwrapped. However, due to the loss of signal and unreliability of the phase outside of the brain, the high-pass filtering method suffers from artifacts at the edges of the brain. Furthermore, studies show that the homodyne high-pass filter affects the phase of the larger structures in the brain and, consequently, QSM underestimates the susceptibility [40].

The Projection onto the Dipole Field (PDF) [41] is another widely used background field removal method. The foundation of the PDF method is based on the observation that the background field induced from outside the region of interest (ROI) is orthogonal to the local field induced by the ROI (except for the voxels near the boundary). PDF is a nonparametric technique that fits the background field to the field induced from the structure outside of the brain or ROI through a minimization formula:

$$\chi_B^* = \underset{\chi_B}{\mathrm{argmin}} \|W(\delta B - d * \chi_B)\|_2, \tag{2.18}$$

where the L-2 norm is calculated over the ROI. W is a weighting matrix calculated from the magnitude image and δB is the total field. The term, $d * \chi_B$ denotes the convolution of the unit dipole kernel, d, and the susceptibility of the region outside of the brain, χ_B. In the next step, the induced background field, δB_B, from the χ_B^* is generated $(d * \chi_B^*)$, and subtracted from δB to get the local field δB_L. The problem of the PDF technique is that the χ_B^* may not reflect the true susceptibility distribution of the region outside the brain [8].

Another well-known background field removal method is Sophisticated Harmonic Artifact Reduction for Phase data (SHARP) [42]. The foundation of SHARP is that the background field can be estimated as a harmonic function of the phase in the homogenous regions. Therefore, it has the spherical mean value property:

$$\Delta B_B = \Delta B_B * S, \tag{2.19}$$

where S is the nonnegative normalized spherical kernel with radius r voxels. Using this property, if Equation (2.17) is subtracted from its convolved version by the spherical kernel and, we have:

$$\Delta B' = \Delta B - \Delta B_B * S = \Delta B_L - \Delta B_L * S. \tag{2.20}$$

This shows that the interim field, $\Delta B'$, only depends on the local field. Therefore, the local field, ΔB_L, can be calculated by deconvolution:

$$\Delta B_L = \Delta B' *^{-1} (\delta - S), \tag{2.21}$$

where $*^{-1}$ denotes the deconvolution, and δ is the unit impulse at the center of the spherical kernel. The radius of the spherical kernel and deconvolution kernel is important in the accuracy of the SHARP. Also, an erosion operation is used in SHARP to remove the voxels at the boundaries of the brain to avoid convolution error in these regions.

2.6   Review of Reconstruction Methods

In the literature, several methods have been proposed to address the ill-posed QSM reconstruction problem. These methods can be categorized into single-orientation and multi-orientation approaches. In the next two sub-sections, we will review some of these methods.

2.6.1   Single-Orientation

The first category belongs to the methods which are based on single-orientation MRI data. The simplest and least time-consuming technique in this category is the Thresholded K-space Division (TKD) approach [43]. TKD is a non-iterative approach that uses a threshold, δ, on the dipole kernel to ignore the smaller values near the zeroes of the dipole kernel in the inversion process:

$$D'(k, \delta) = \begin{cases} \frac{1}{3} - \frac{k_z^2}{k^2}, & if \ \left| \frac{1}{3} - \frac{k_z^2}{k^2} \right| > \delta \\ sgn\left(\frac{1}{3} - \frac{k_z^2}{k^2} \right).\delta, & otherwise \end{cases}. \tag{2.22}$$

Although TKD is a fast method, the reconstructed susceptibility map using this method suffers from streaking artifacts and underestimates χ, especially around the structures with high susceptibilities such as midbrain structures and veins.

An alternative approach referred to as iterative Susceptibility Weighted Imaging and Mapping (iSWIM) [21] is a post-processing on the reconstructed susceptibility map by TKD. iSWIM applies the geometrical-based constraints on the reconstructed QSM iteratively to fill in the missing parts of the k-space in every iteration. This is accomplished by constraining the susceptibility values in regions with high susceptibility and, therefore, reducing the streaking artifact around these structures.

Another group of approaches in the single-orientation category use regularization techniques with different *a priori* information to reconstruct the susceptibility map. Although these methods are computationally more expensive than TKD and iSWIM approaches, the reconstruction times are still reasonable. These methods are designed to smooth over regions that have homogeneous susceptibilities. For example, morphology enabled dipole inversion (MEDI) exploits the structural consistency between χ and the magnitude image in the form of an ℓ_1-norm [44]:

$$\chi_{MEDI} = \underset{\chi}{\operatorname{argmin}} \ \lambda \|W(F^{-1}DFX - \delta B)\|_2^2 + \|MG\chi\|_1, \tag{2.23}$$

where W is a weighting matrix proportional to the magnitude image; λ and G denote the Lagrange multiplier and the gradient operators. M is extracted from the gradient of the magnitude image. Therefore, MEDI reconstructs QSMs with smooth homogenous regions while the edges that were derived from the magnitude image are preserved. However, this constraint can cause errors in regions where there are inconsistencies between the magnitude images and the susceptibility maps. Homogeneity Enabled Incremental Dipole Inversion (HEIDI) [23] is similar to MEDI, but it uses structural information from both magnitude and phase images to correct this issue.

An alternative approach, structural feature-based collaborative reconstruction (SFCR) [24], argues that the edge information from either magnitude or phase images does not reflect all the structural features in χ and the reconstructed image suffers from over-smoothed edges. The key steps in SFCR are to include a structural feature-based ℓ_1-norm constraint and a voxel fidelity-based ℓ_2-norm constraint. This iterative approach contains two separate steps: the M-step and the S-step.

$$\text{M-step: } \tilde{\chi} = \underset{\chi}{\text{argmin}} \, \lambda_1 \|\chi_k(k)H - diag(H)F\chi\|_2 + \|P_{mag}\nabla\chi\|_1 + \lambda_2\|R_1\chi\|_2, \text{ and} \qquad (2.24)$$

$$\text{S-step: } \chi_{SFCR} = \underset{\chi}{\text{argmin}} \, \gamma_1\|W(\delta B - C\chi)\|_2 + \|P_{\tilde{\chi}}\nabla\chi\|_1 + \gamma_2\|R_2\chi\|_2, \qquad (2.25)$$

where in the M-step, $\chi_k(k) = C_k(k)^{-1}\delta B_k(k)$ and $C_k(k)$ is the unite dipole kernel. H is the mask to determine the ill-conditioned versus well-conditioned elements of the dipole kernel. P_{mag} is the binary mask from thresholding the gradient of magnitude images, and

R_1 is the binary mask that determines the high and low SNR regions. In S-step, $C = F^{-1}C_k(k)F$, and W is the weighting matrix that determines the reliability of the data. Furthermore, $P_{\tilde{\chi}}$ is the binary mask from thresholding the gradient of the output of M-step, $\tilde{\chi}$, and R_2 is a mask segmenting the image into three regions with low SNR, high SNR, and artifact. Also, λ_1, λ_2, γ_1, and γ_2 are the Lagrange multipliers for the M- and S-steps. SFCR was reported to be able to recover both edges and small objects while still minimizing artifacts. However, it involves solving two minimization problems and finding the optimal values for four parameters.

It is important to mention that most of these methods find the local normalized field, δB, through a linear fitting of multi-echo phase data. However, the inclusion of long echo times can lead to blooming artifacts, an increase in signal loss at the edges of the object and, potentially, an underestimation of χ. We will discuss this in more detail in the next chapter when introducing multi-echo scSWIM.

In addition to the above mentioned methods, in recent years, there have been efforts to introduce deep neural networks to address the ill-posed QSM reconstruction inverse problem. QSMnet [45] and DeepQSM [46] are examples of these methods. QSMnet takes advantage of the modified U-Net architecture, and Deep QSM uses a convolutional deep neural network. However, beside the need for these methods for large training datasets, the performance of these approaches in cases with abnormalities still needs further investigation.

2.6.2 Multi-Orientation

This group of methods utilizes multiple scans that are acquired at different head orientations. One of the most used methods in this category is the Calculation Of Susceptibility through Multiple Orientation Sampling (COSMOS) [25]. This method utilizes the phase images from multiple orientations to stabilize the inversion process and remove the singularities by weighted linear least squares. That is, assuming that the $\Delta B_1(k)$, $\Delta B_2(k)$, …, and $\Delta B_N(k)$ are the local fields in k-space, the COSMOS is trying to solve the following equation:

$$\begin{bmatrix} \Delta B_1(k) \\ \Delta B_2(k) \\ \vdots \\ \Delta B_N(k) \end{bmatrix} = \chi(k) \begin{bmatrix} D(k,\theta_1) \\ D(k,\theta_2) \\ \vdots \\ D(k,\theta_N) \end{bmatrix}, \tag{2.26}$$

where $D(k,\theta_i) = \frac{1}{3} - \frac{(k_z \cos\theta_i + k_y \sin\theta_i)^2}{k^2}$ is the unit dipole kernel in k-space for the scan with the rotation of θ_i degree from the main magnetic field, where θ_i is the angle between k_z and B_0.

Although the multi-orientation approaches are promising in theory, they are not practical for clinical applications due to the acquisition of multiple scans. Furthermore, perfect registration between multiple orientations is needed to avoid misregistration errors and that can be challenging. Additionally, further investigation is required to study the effects of the microstructures with anisotropic susceptibility on the reconstructed

26

COSMOS since this method averages the contributions from these structures [47]. Nonetheless, apart from perfect simulation data, COSMOS is usually used as a gold standard in the evaluation of any single-orientation QSM reconstruction method.

3 Methods

In this chapter, the theory and implementation of the proposed scSWIM approach are discussed in detail. Then, the framework to obtain the multi-echo scSWIM from STAGE imaging is explained. Additionally, the simulated and *in vivo* test datasets are reviewed.

3.1 Single-Echo scSWIM

As mentioned in Section 2.4, the relationship between the normalized local field, δB, and the susceptibility map, χ, in GRE imaging is given as:

$$\delta B = F^{-1}DF\chi, \tag{3.1}$$

where F and F^{-1} denote the Fourier and inverse Fourier transform operators, respectively; and D is the Fourier transform of the unit dipole function in k-space introduced in Equation (2.12). Based on these notations, the objective function of scSWIM is formulated as:

$$f(\chi) = \frac{1}{2}\|W(F^{-1}DF\chi - \delta B)\|_2^2 + \lambda_1\|PG\chi\|_1 + \frac{\lambda_2}{2}\|R\chi\|_2^2, \tag{3.2}$$

and the final solution for the susceptibility is given by:

$$\chi_{scSWIM} = \underset{\chi}{argmin}\, f(\chi). \tag{3.3}$$

The objective function of scSWIM includes a data fidelity term along with two regularization terms: the first one is based on an ℓ_1-norm measure and the second one is

based on an ℓ_2-norm measure. The W in the data fidelity term denotes a weighting matrix proportional to the magnitude image that defines the reliability of the magnetic field change from the background field for each voxel. Also, G in the ℓ_1-norm regularization term is the gradient operator.

The objective function of scSWIM is similar to the S-step of SFCR [24] with changes in constraints. As discussed in Section 2.6.1, in the S-step of the SFCR method, the edge matrix, P, is a binary mask that is derived from the initial susceptibility, $\hat{\chi}$. This initial $\hat{\chi}$ is reconstructed from the first regularized minimization step, called the M-step. The M-step is based on an objective function that is similar to the S-step, but its constraints are based on the magnitude image. Also, R in the S-step of the SFCR method is a fidelity mask where voxels with high signal-to-noise ratio (SNR) are mapped to zero, low SNR to one and voxels corresponding to susceptibility artifact to two. However, the choice of R, P, and the starting input are different for scSWIM as described below.

In scSWIM, we replaced the SFCR first regularized minimization (M-step) with iSWIM [21] since it is fast, has no smoothing, and provides an initial susceptibility map with sharp vessels. Then, in the ℓ_1 regularization term of Equation (3.2), we used the edge matrix, P, which is the binary mask that is derived from the product of the thresholded gradients of the STAGE T1WE image, P_{T1WE}, and the initial susceptibility map, $P_{\hat{\chi}}$:

$$P_{T1WE,i} = \begin{cases} 0, & |G_i\rho| \geq \mu_1 \\ 1, & |G_i\rho| < \mu_1 \end{cases} \quad \text{and} \quad P_{\hat{\chi},i} = \begin{cases} 0, & |G_i\hat{\chi}| \geq \mu_2 \\ 1, & |G_i\hat{\chi}| < \mu_2 \end{cases}, \tag{3.4}$$

where ρ denotes the STAGE T1WE image which was discussed in Section 2.2. Also, G_i denotes the gradient operator in the direction of i which is an indicator of the x, y, or z directions. Both μ_1 and μ_2 are threshold values chosen to be 2.5 times the noise level of the derivatives of ρ and $\hat{\chi}$, respectively, in order to maintain the edges of the gray/white matter, veins, and other structures in the brain. Essentially, P_{T1WE} excludes the edges of the white matter and gray matter and $P_{\hat{\chi}}$ excludes the edges of the vessels and basal ganglia structures and $P = P_{T1WE} \times P_{\hat{\chi}}$.

In the ℓ_2 regularization term, we have used a structural matrix R to protect voxels in the regions of high susceptibilities, such as veins and basal ganglia structures, from being over-smoothed while still smoothing other regions. The matrix R is generated from the normalized T1WE image, excluding the regions detected in the R_{DGM} (where DGM stands for "deep gray matter") and $R_{\hat{\chi}}$ masks defined next. The R_{DGM} mask is calculated using an atlas-based segmentation method developed in-house [48]. This method segments the deep gray matter structures from the high flip angle magnitude image (T1W), STAGE T1WE data, initial susceptibility, and T1 maps. The $R_{\hat{\chi}}$ mask is generated from the method used in [21] by applying a threshold to the homodyne filtered $\hat{\chi}$ map. Finally, the constants λ_1 and λ_2 are found using the L-curve approach [49].

Both the ℓ_1- and ℓ_2-norm based regularization terms in scSWIM are attempting to smooth the homogenous regions. For the gradient of the susceptibility map, the ℓ_1-norm is used to impose the sparsity constraint. That is because the optimum solution for χ should

result in a sparse $PG\chi$. On the other hand, the $R\chi$ using for the optimum χ will result in a map with remaining low susceptibility values since the R mask has already excluded the high susceptibility regions. Therefore, it is not a sparse matrix and the sparsity constraint is not needed here; hence the ℓ_2-norm is used for this regularization term.

For solving the problem of minimization of the scSWIM objective function in Equation (3.2), we use the split-Bregman method [50]. This method solves the ℓ_1 regularized minimization problem by splitting it and then solving using Bregman iteration. Therefore, assuming $y \triangleq PG\chi$, Equation (3.2) is reformulated as:

$$(\chi_{scSWIM}, \hat{y}) = \underset{(\chi,y)}{\mathrm{argmin}} \left\{ \frac{1}{2} \|W(F^{-1}DF\chi - \delta B)\|_2^2 + \lambda_1 \|y\|_1 + \frac{\lambda_2}{2} \|R\chi\|_2^2 \right\} \ \text{s.t.} \ y = PG\chi. \tag{3.5}$$

Using quadratic penalty, we can rewrite the above equation as:

$$(\chi_{scSWIM}, \hat{y}) = \underset{(\chi,y)}{\mathrm{argmin}} \left\{ \frac{1}{2} \|W(F^{-1}DF\chi - \delta B)\|_2^2 + \lambda_1 \|y\|_1 + \frac{\lambda_2}{2} \|R\chi\|_2^2 + \right. \tag{3.6}$$

$$\left. \frac{\mu}{2} \|PG\chi - y + \eta\|_2^2 \right\}.$$

Then, using the Bregman iteration technique [51], this equation can be solved in the form of two iterative optimization subproblems and Bregman updates as the following iterative sequence:

$$\chi^{(k)} = \underset{\chi}{\mathrm{argmin}} \left\{ \frac{1}{2} \|W(F^{-1}DF\chi - \delta B)\|_2^2 + \frac{\lambda_2}{2} \|R\chi\|_2^2 + \frac{\mu}{2} \|PG\chi - y^{(k-1)} + \eta^{(k-1)}\|_2^2 \right\}, \tag{3.7}$$

$$y^{(k)} = \underset{y}{\mathrm{argmin}} \left\{ \lambda_1 \|y\|_1 + \frac{\mu}{2} \|PG\chi^{(k)} - y + \eta^{(k-1)}\|_2^2 \right\}, \text{ and} \tag{3.8}$$

31

$$\eta^{(k)} = \eta^{(k-1)} + \left(PG\chi^{(k)} - y^{(k)}\right), \tag{3.9}$$

where the superscripts $(k-1)$ and (k) denote $k - 1^{\text{th}}$ and k^{th} iterations. The Bregman update in Equation (3.9) updates η to introduce back the inconsistency between $PG\chi$ and y after each iteration. In the following material, we will show how to solve the two optimization subproblems.

Equation (3.7) can be solved by taking the derivative of its objective function with respect to χ (considering y and η are constants) and setting it to zero:

$$(F^{-1}D^T FW^T)\left(WF^{-1}DF\chi^{(k)} - W\delta B\right) + \lambda_2 R^T R\chi^{(k)} + \mu G^T P^T\left(PG\chi^{(k)} - y^{(k-1)} + \eta^{(k-1)}\right) = 0, \tag{3.10}$$

where the superscript T denotes the transpose matrix. The gradient operator G can be defined as $G = F^{-1}EF$ based on the gradient operator in the frequency domain, $E = [E_x, E_y, E_z]$, in which $E_x = 1 - e^{-2\pi i k_x/N_x}$, $E_y = 1 - e^{-2\pi i k_y/N_y}$, and $E_z = 1 - e^{-2\pi i k_z/N_z}$ for the matrix size of $[N_x, N_y, N_z]$. Therefore, we can rewrite and simplify the equation in the form of:

$$(D^T FW^2 F^{-1}D + \lambda_2 FR^2 F^{-1} + \mu E^T FP^2 F^{-1}E)F\chi^{(k)} = D^T FW^2 \delta B + \tag{3.11}$$
$$\mu E^T FP^T\left(y^{(k-1)} - \eta^{(k-1)}\right),$$

where this equation is in the form of Ax=b and can be solved using the preconditioned conjugate gradient solver [52]. Therefore, the solution for Equation (3.7), is in the form of:

$$\chi^{(k)} = F^{-1}(D^T F W^2 F^{-1} D + \lambda_2 F R^2 F^{-1} + \mu E^T F P^2 F^{-1} E)^{-1}(D^T F W^2 \delta B + \qquad (3.12)$$

$$\mu E^T F P^T (y^{(k-1)} - \eta^{(k-1)})).$$

The second subproblem stated in Equation (3.8) can be solved using the soft-thresholding [53]:

$$y^{(k)} = max\left(\left| P G \chi^{(k)} + \eta^{(k-1)} \right| - \tfrac{\lambda_1}{\mu}, 0 \right) sgn(G\chi^{(k)} - y^{(k-1)} + \eta^{(k-1)}). \qquad (3.13)$$

Therefore, solving Equation (3.2) at the kth iteration has three steps: first, finding $\chi^{(k)}$ through Equation (3.12); then, calculating $y^{(k)}$ through Equation (3.13) using the newly calculated $\chi^{(k)}$; and finally, finding $\eta^{(k)}$ via Equation (3.9) using the calculated $\chi^{(k)}$ and $y^{(k)}$. This process can be iterated to reach the best reconstruction when the changes in the reconstructed QSM image in two recent iterations is below a certain threshold. The summary of the scSWIM process is shown in Algorithm 3.1.

3.2   Multi-Echo scSWIM for STAGE

The single-echo scSWIM approach described in the previous section was then adopted to handle the multiple echo, multiple flip angle STAGE data. For this purpose, the QSM image that is reconstructed by the iSWIM method [21] was used as the initial input into scSWIM for the low flip angle, short echo STAGE data (FA$_L$TE$_1$) . Then, for the other three echoes from the STAGE data (FA$_H$TE$_1$, FA$_L$TE$_2$, and FA$_H$TE$_2$), the reconstructed scSWIM from the previous echo was used as the initial guess for processing the scSWIM

Algorithm 3.1. Single-echo scSWIM procedure

Input	:	δB	Normalized local field (preprocessed GRE phase data)
		χ^0	Initial susceptibility map from iSWIM
		W	Weighting matrix
		P	Edge map in three directions ($P = [P_x, P_y, P_z]$)
		R	Structural mask
		λ_1, λ_2	scSWIM regularization parameters
		μ	Intermediate parameter used for solving the ℓ_1 regularization term
		M_χ	Maximum number of scSWIM iterations
		M_{PCG}	Maximum number of PCG iterations
		ε_χ	Maximum tolerance of scSWIM iterations
		ε_{PCG}	Maximum tolerance of PCG iterations
Output	:	$\chi^{(k)}$	Reconstructed QSM using scSWIM algorithm

1 : $\textbf{\textit{function }} scSWIM(\delta B, \chi^0, W, P, R, \lambda_1, \lambda_2, \mu, M_\chi, M_{PCG}, \varepsilon_\chi, \varepsilon_{PCG})$

2 : $y^{(0)} \leftarrow 0$

3 : $\eta^{(0)} \leftarrow 0$

4 : **for** $k = 1 \rightarrow M_\chi$ **do**

5 : calculate $\chi^{(k)}$ from Equation (3.12) using PCG:
$$\chi^{(k)} \leftarrow PCG(W, R, P, \delta B, D, y^{(k-1)}, \eta^{(k-1)}, \mu, \lambda_2, M_{PCG}, \varepsilon_{PCG})$$

6 : calculate $y^{(k)}$ from Equation (3.13):
$$y^{(k)} = max\left(\left|PG\chi^{(k)} + \eta^{(k-1)}\right| - \frac{\lambda_1}{\mu}, 0 \right) sgn(G\chi^{(k)} - y^{(k-1)} + \eta^{(k-1)})$$

7 : Calculate $\eta^{(k)}$ from Equation (3.9):
$$\eta^{(k)} \leftarrow \eta^{(k-1)} + (PG\chi^{(k)} - y^{(k)})$$

8 : $\Delta\chi \leftarrow \left\|\chi^{(k)} - \chi^{(k-1)}\right\|_2^2 / \left\|\chi^{(k-1)}\right\|_2^2$

9 : **if** $\Delta\chi < \varepsilon_\chi$ **then**

10 : **return** $\chi^{(k)}$

11 : **end if**

12 : $\chi^{(k-1)} \leftarrow \chi^{(k)}$

13 : **end for**

14 : **end function**

of the next echo. Finally, an averaged scSWIM was generated by using an R_2^*-based weighted average of the individual echo scSWIM (χ_i) results:

$$\chi = \frac{\sum_i w_i^2 \chi_i}{\sum_i w_i^2},$$
(3.14)

where $w_i = TE_i e^{-TE_i R_2^*}$ and R_2^* is calculated from the STAGE data that was discussed in Section 2.2. In regions with smaller susceptibility values, the weighting will be larger for longer echoes. On the other hand, the weighting will be larger for the shorter echoes in high susceptibility regions. Additionally, the weighting w_i will be maximized when $TE_i = 1/R_2^* = T_2^*$.
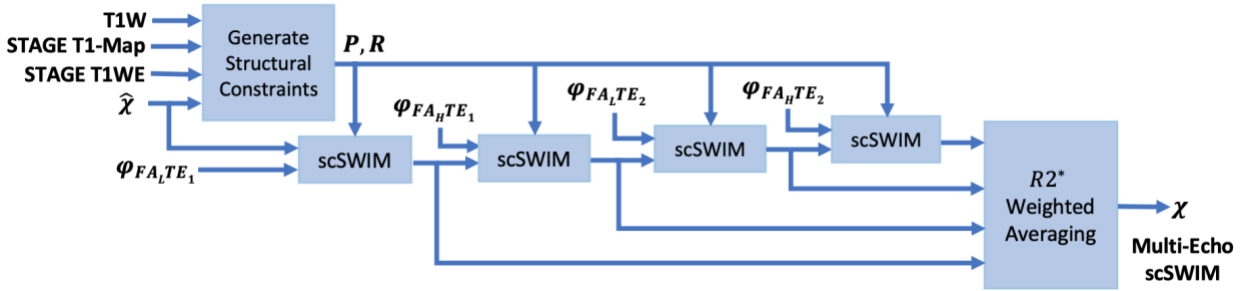
Figure 3.1. Block diagram of multi-echo, multi-flip angle scSWIM for STAGE imaging. Here, $\boldsymbol{\varphi}$, $\hat{\boldsymbol{\chi}}$ denote the phase and initial estimate of the susceptibility map from the multi-echo R2* weighted iSWIM, respectively. FA$_L$ and FA$_H$ denote the double-echo low and high flip angles scans of STAGE imaging, respectively.

This multi-echo approach has three advantages: first, each echo can be reviewed; second, the weighted scSWIM will have a better SNR; and third, loss of tissues associated with the use of a phase quality control map (especially at longer echoes) will be, to a large degree, replaced with the shorter echo scSWIM value. This weighting automatically ensures that wherever there is a measured susceptibility from one echo it will contribute to the final QSM result (while echoes with zeroes will not make a contribution). Figure 3.1 shows the block diagram of the proposed multi-echo, multi-flip angle scSWIM processing steps for STAGE.
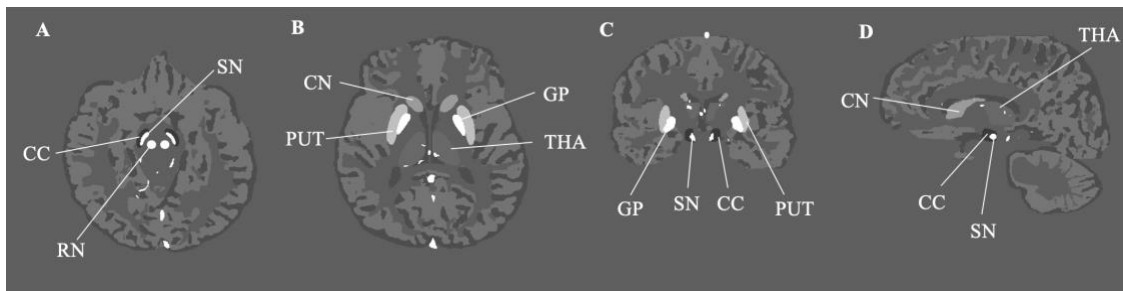
Figure 3.2. Illustration of the human brain model in the axial (**A** and **B**), coronal (**C**), and sagittal (**D**) views showing the deep gray matter structures such as GP (Globus Pallidus), PUT (Putamen), THA (Thalamus), CN (Caudate Nucleus), SN (Substantia Nigra), RN (Red Nucleus), and CC (Crus Cerebri).

3.3 Simulated Data

The 3D isotropic susceptibility model developed in [54] was used to test the scSWIM algorithm. This model includes the general structures of the human brain such as gray matter (GM), white matter (WM), cerebrospinal fluid (CSF), the major veins, and basal ganglia and midbrain structures such as globus pallidus (GP), putamen (PUT), thalamus (THA), caudate nucleus (CN), substantia nigra (SN), red nucleus (RN), and crus cerebri (CC) (see Figure 3.2). The susceptibility values for these structures are summarized in the first row of Table 3.1. Additionally, to test the performance of the reconstruction in the presence of cerebral microbleeds (CMB) or calcium deposits (CaD), two spherical objects with susceptibility values (radius) of 1000 ppb (5 mm) and 3000 ppb (3 mm), respectively, were added to the frontal white matter and two spherical objects with susceptibility values of -1000 ppb (5 mm) and -3000 ppb (3 mm) were added to the posterior white matter. Also, one spherical object with a radius of 3 mm with susceptibility of -3000 ppb was added to the model to mimic the pineal gland (PG). The values for CMBs were taken from our experience in the field of traumatic brain injury and stroke where we usually see CMBs with susceptibilities as large as 1000 ppb but on occasion higher values up to 2000 ppb and 3000 ppb have been seen, so both 1000 ppb and 3000 ppb were used to test the metal of the method. For the CaD, the values are around -3000 ppb but can range lower and slightly higher than this as the calcium is highly diamagnetic [55].

This final susceptibility model, χ_{ideal}, was used to generate the magnitude and phase images using the STAGE imaging parameters: FA=6°/24°, TE$_1$=7.5/8.75ms,

TE$_2$=17.5/18.75ms, and TR=25ms. The phase images were simulated from the forward model in Equation (2.8) at B$_0$=3T.

To create the magnitude images, first, the R2* map was generated from χ_{ideal} using the relationship R2* = 20/s + 0.125χ [14] except for the CMB, PG, and CaD objects R2* was set to 40/s. Then, the magnitude image was calculated using the Ernst equation discussed in Equation (2.6). The proton density and T$_1$ relaxation times for different brain structures are summarized in Table 3.1. These values were adopted from the literature [22,50] or manually measured from the in-vivo STAGE PD-map and T1-map. For CMB, PG, and CaD objects, the proton density was assumed to be zero which led to no signal in these regions.

Table 3.1 Susceptibility, T$_1$ relaxation time, and relative proton density ($\boldsymbol{\rho_0}$) values for different structures in the simulated brain model.

	WM	GM	GP	PUT	THA	CN	SN	RN	CC	V	VNT/CSF
$\boldsymbol{\chi}$ **(ppb)**	0	20	180	90	10	60	160	130	-30	450	-14
$\mathbf{T_1}$ **(ms)**	837	1607	888	1140	1218	1226	1147	833	780	1932	4163
$\boldsymbol{\rho_0}$	0.73	0.80	0.72	0.82	0.79	0.82	0.79	0.80	0.79	0.85	1.00

WM (white matter), GM (gray matter), GP (Globus Pallidus), PUT (Putamen), THA (Thalamus), CN (Caudate Nucleus), SN (Substantia Nigra), RN (Red Nucleus), CC (Crus Cerebri), V (Veins), VNT (Ventricles), CSF (Cerebrospinal Fluid), and ppb (parts per billion).

Finally, Gaussian noise was added to the complex signal to produce an SNR of 10:1 with respect to white matter. The reconstructed susceptibility map using the proposed method was compared with the TKD, iSWIM, and MEDI methods. The original simulated susceptibility model (χ_{ideal}) was used as the gold standard to measure the performance of each method using Root Mean Squared Error (RMSE) and Structural Similarity Index Metrics (SSIM) as measures of goodness of fit [57] where SSIM=1 corresponds to the perfect structural similarity while SSIM=0 indicates no similarity between the two images.

3.4 In Vivo Data

The proposed scSWIM method was also tested on two sets of in vivo datasets. All subjects involved in this study signed a consent form to be scanned.

3.4.1 Single Case with Multiple Orientations

The *in vivo* MRI data for a single test case was acquired from a 29-year old male volunteer on a 3T Siemens scanner (Siemens Healthcare, Erlangen, Germany) at Wayne State University. The imaging parameters were: 6º and 24º for the low and high flip angle scans with TR=25ms, TE$_1$= 6.5/7.5ms, TE$_2$=17.5/18.5ms, bandwidth: 277Hz/pixel, and GRAPPA=2. The matrix size, voxel resolution, and FOV were 384×288×104,

$0.67 \times 0.67 \times 1.33 \text{mm}^3$, and $256 \times 192 \times 139 \text{mm}^3$, respectively. The total scan time for the high-resolution STAGE was about 10 minutes.

For the purpose of generating COSMOS, two additional orientations with the same imaging parameters were collected for this subject. The reconstructed susceptibility map using the proposed scSWIM method was compared with those from the TKD, iSWIM, and MEDI methods and compared to COSMOS as the reference image.

3.4.2 A Set of Healthy Controls versus Parkinson's Disease Patients

Additionally, we tested scSWIM on a cohort of Parkinson's disease (PD) patients and healthy controls (HC) acquired using a Siemens 3T Prisma scanner with lower resolution compared to the above-mentioned *in vivo* case. The imaging parameters were the same for the sample used above in the simulated data except for the matrix size, voxel resolution, and FOV were $384 \times 144 \times 64$, $0.67 \times 1.33 \times 2 \text{mm}^3$ (interpolated to $0.67 \times 0.67 \times 2 \text{mm}^3$) and $256 \times 192 \times 128 \text{mm}^3$, respectively, $TE_1 = 7.5/8.5 \text{ms}$, and a bandwidth of 240Hz/pixel. The total scan time for this resolution was about 5 minutes. A total of 20 subjects were evaluated: 10 PD patients (62.6 ± 8.5 years old) and 10 HC subjects (62.6 ± 8.4 years old) that are age and sex-matched.

3.5   Data Pre-Processing

The entire processing pipeline was implemented in MATLAB (The Mathworks, Inc, Natick, MA, USA) on a workstation with Windows 10, Intel CPU i7-3770 with four cores and 16GB RAM.

For the *in vivo* data, the brain mask was extracted from the magnitude images using BET [34] as discussed in Section 2.5.12.5.3. Then, the phase image was unwrapped using the bootstrapping [38] and quality guided 3D phase unwrapping [36] methods (Section 2.5.2) in the simulated and *in vivo* data, respectively. Next, the induced background field from the air/tissue interfaces in the *in vivo* data was removed from the unwrapped phase using SHARP algorithm [42] (Section 2.5.3) with a kernel size of 6 pixels. Finally, the resulting phase was zero-padded symmetrically in the spatial domain to a matrix size of 256×256×256 or 512×512×512 for simulated and *in vivo* datasets, respectively.

3.6   Susceptibility Map Reconstruction

The scSWIM parameters λ_1 and λ_2 in Equation 3.2) were determined by plotting the measured residual errors of the data fidelity and the two regularization terms for each of the individual STAGE scans using the L-curve method [49]. In theory, λ_1 controls the spatial smoothness and λ_2 helps to preserve the high susceptibility regions and small objects such as vessels from being over-smoothed.

As mentioned in Section 3.1, an atlas-based segmentation method developed in-house [48] was used to generate the R_{DGM} mask. This method provided the labeled mask segmenting the right and left subcortical deep gray matter structures from the T1W, STAGE T1WE, T1 map, and $\hat{\chi}$. This labeled mask was carefully reviewed and if needed fine-tuned manually (this was done on 6 cases for the GP and SN structures which sometimes were smaller than what would have been drawn manually). If these regions had not been corrected, the algorithm would have smoothed that part of the GP not protected. Finally, the R_{DGM} mask was generated from binarizing the labeled mask.

Several algorithms were chosen to compare with scSWIM, including TKD, iSWIM, and MEDI. In generating the MEDI results, a regularization parameter of 250 (350) was used for the simulated (*in vivo*) data. For TKD processing, a threshold of 0.1 was used and iSWIM was performed with 4 iterations. All of these parameters were adjusted to give the lowest RMSE. Additionally, COSMOS was used as the gold standard for the *in vivo* data. Multi orientation images for the COSMOS data were co-registered using ANTs [52, 53]. In the TKD, iSWIM, and scSWIM methods, the final multiple echo, multiple flip angle QSM data were generated using a multi-echo R2*-based weighted averaging of the individual QSM images from each echo and each flip angle data. In MEDI, the final QSM was generated by averaging the reconstructed QSM images from the fitted phases in each of the multi-echo low and high flip angle scans.

3.7 Quantitative Analysis of the Susceptibility Maps

For the quantitative analysis of the data, the susceptibility mean and standard deviation were found from the entire 3D structure of interest. In the simulated model, all the structures of interest were measured automatically (since we know the location of each structure). For the *in vivo* data, the susceptibility of the midbrain structures was also automatically measured since they have been determined in creating the R_{DGM} masks for the boundaries of these structures as described earlier. On the other hand, the susceptibility of the CSF, WM, and major veins (SSV) and internal cerebral vein (ICV) were measured manually by tracing the ROIs on the QSM data using SPIN (SpinTech, Inc. Bingham Farms, MI. USA). The manual tracing was performed in the axial view for CSF and WM, but veins were traced in the sagittal view for easier localization. A linear regression model was used to compare the measured susceptibility values from each reconstruction method with those from the susceptibility model and COSMOS to assess the accuracy of midbrain structures in the simulated and *in vivo* data, respectively.

4 Results

4.1 Simulated Data

By comparing the P and R masks for the simulated data (discussed in Section 3.3) and also the first and second regularization terms, and for the purpose of bringing the two terms to the same order, we set $\lambda_1 = 0.005\lambda_2$. This is further reviewed in the Discussion section. Based on this assumption and simulations in the human brain model, $\lambda_2 = \{6.81, 1.47, 3.16, 1.00\} \times 10^{-3}$ provided the best results in terms of residual errors for the four different scans (FA$_L$TE$_1$, FA$_H$TE$_1$, FA$_L$TE$_2$, and FA$_H$TE$_2$), respectively (see Figure 4.1A-C for FA$_H$TE$_1$).

A comparison of scSWIM with TKD, iSWIM, and MEDI, along with their absolute errors and structural similarity maps relative to the simulation model is shown in Figure 4.2. In the simulated data (Figure 4.2A-C), we have used the exact known edge and structural matrices from χ_{ideal} to create P_{ideal} (Figure 4.2D) and R_{ideal} (Figure 4.2E). The TKD results (Figure 4.2F-J) show severe streaking artifacts while the iSWIM results have much less streaking (Figure 4.2K-O). MEDI does an excellent job (Figure 4.2P-T), as does scSWIM (Figure 4.2U-Y) in reproducing the model with minimal artifacts and noise. In both these last two reconstructions, the streaking artifact is highly reduced compared to both TKD and iSWIM, and the images look much better in terms of SNR. However, MEDI

does not resolve the streaking artifact from the CMBs, pineal gland, or calcified objects

with higher susceptibility values.
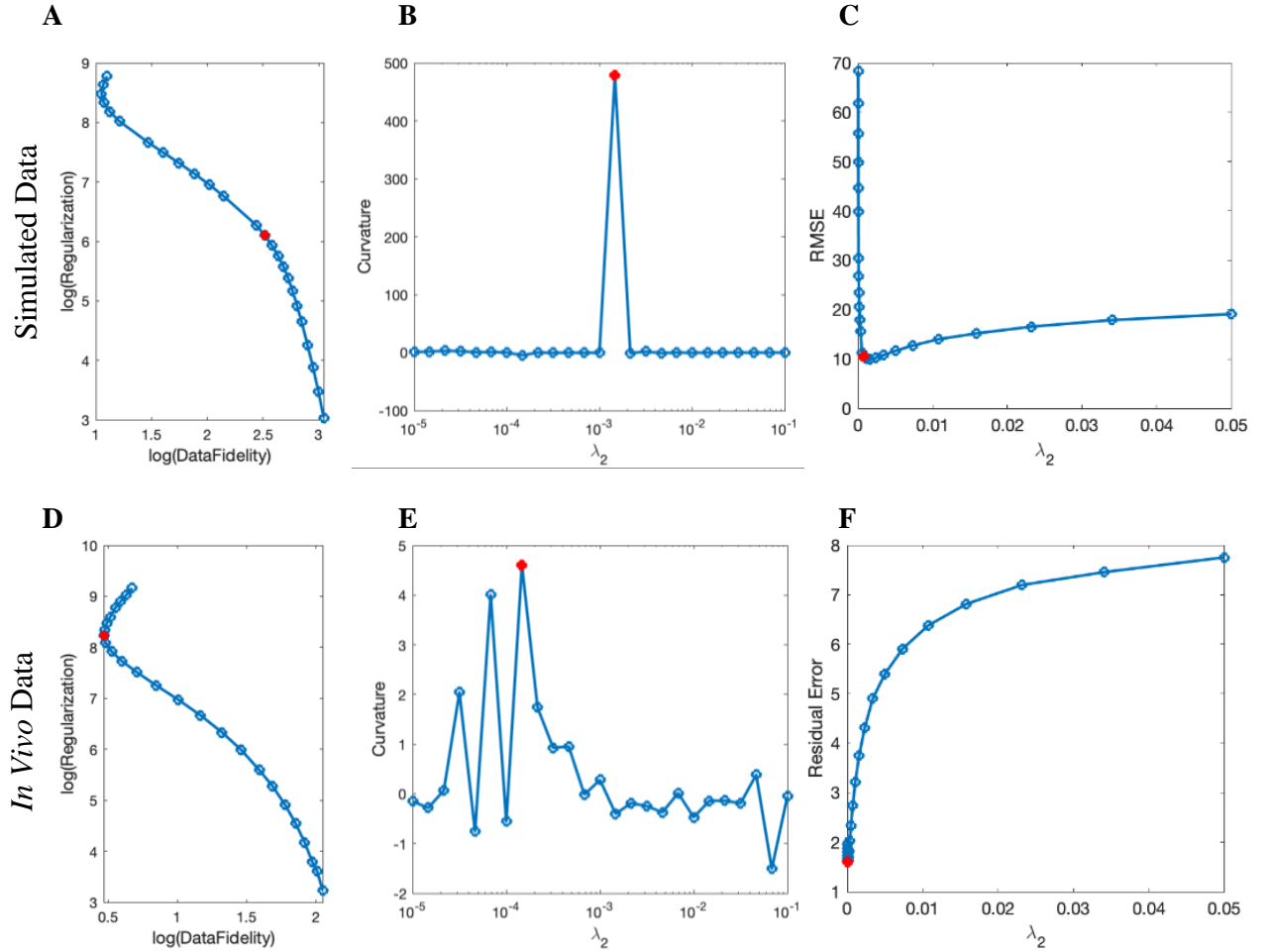
Figure 4.1. Determination of the scSWIM regularization parameter λ_2 in the simulated (**A-C**) and *in vivo* (**D-F**) data for the higher flip angle, short echo (FA$_H$TE$_1$) scan using the L-curve method. The curves in the first column show the log-log L-curve. The curvature and RMSE/residual error plot vs. λ_2 values are displayed in the third column. The optimal values (shown by the red circle) for the scSWIM at FA$_H$TE$_1$ scan were determined to be $\lambda_2 = 1.47 \times 10^{-3}$ and $\lambda_2 = 1.47 \times 10^{-4}$ for the simulated and *in vivo* data, respectively, where λ_1 was set equal to $0.005\lambda_2$. This process is repeated for the other scans (FA$_L$TE$_1$, FA$_L$TE$_2$, and FA$_L$TE$_2$) and the optimal parameters were selected.

In the simulated data with (or without) CMBs, PG, and CaDs, the RMSE for TKD, iSWIM, MEDI, and scSWIM were 32.91 (22.09), 24.61 (18.21), 47.53 (8.74), and 5.01 (5.21) ppb, respectively. Also, the SSIM index was measured as 0.52 (0.59), 0.62 (0.63), 0.80 (0.86) and 0.90 (0.91) for TKD, iSWIM, MEDI, and scSWIM, respectively, for these two conditions. Based on these results, scSWIM has the lowest error and the highest similarity to the model compared to the other methods. The measured susceptibility values in different structures are summarized in Table 4.1 showing that the measured susceptibilities in the midbrain structures for both MEDI and scSWIM are closer to the expected susceptibilities in the model while scSWIM has smaller standard deviations. The measured susceptibilities of the straight sinus vein, calcium deposition and CMBs show that scSWIM provides the most accurate results in these structures as well.
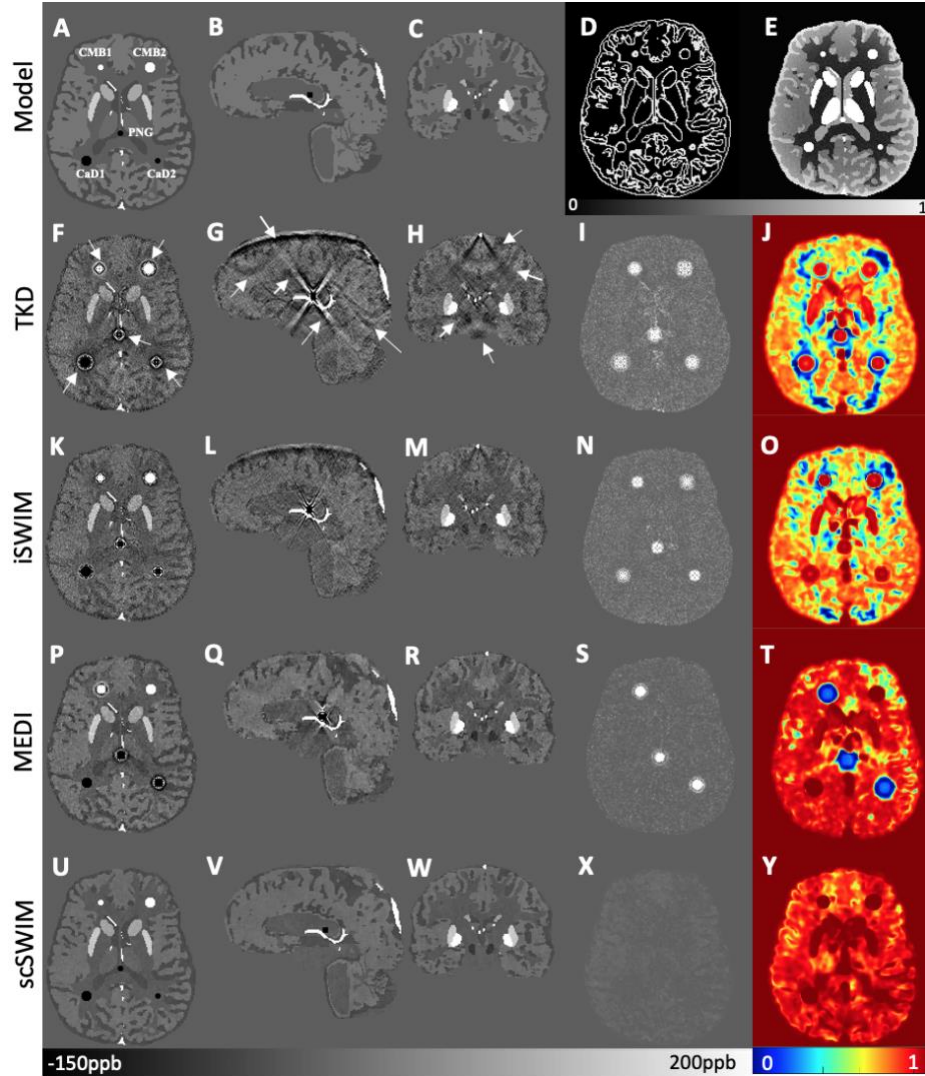
Figure 4.2. Depiction of multi-echo, multi-flip angle QSM images using different methods for the simulated data. This figure shows the orthogonal views of the susceptibility model (**A-C**), and reconstructed QSM images from TKD (**F-H**), iSWIM (**K-M**), MEDI (**P-R**), and scSWIM (**U-W**) along with the scSWIM constraints P_{ideal} (**D**) and R_{ideal} (**E**). The cerebral microbleeds (CMB), pineal gland (PG) and calcium deposits (CaD) are labeled on the model (**A**). Streaking artifacts are indicated by the arrows. The last two columns show the corresponding susceptibility absolute error map (**I,N,S,X**) and structural similarity map (**J,O,T,Y**) for the different methods. In this simulated data, scSWIM provides better reconstruction with less artifacts, less error, and higher similarity relative to the numerical model. Please note that the complements of the P and R masks are shown in this figure (**D,E**) for better visualization.

Table 4.1 Measured susceptibility values (mean ± standard deviation) in ppb for different structures in the reconstructed QSM images using TKD, iSWIM, MEDI, and scSWIM methods for the simulated human dataset along with the reference values. The susceptibilities for the left and right CN, GP, PUT, THA, RN, SN, and CC were measured.

Regions	TKD	iSWIM	MEDI	scSWIM	Model
CN-L	44.17±18.22	49.65±15.46	54.55±9.46	55.92±2.41	60.00
CN-R	44.19±18.67	49.19±15.24	53.74±9.94	55.42±2.23	60.00
GP-L	152.17±22.03	167.80±18.41	172.06±9.64	177.50±2.74	180.00
GP-R	151.02±20.65	166.44±17.05	174.20±9.93	175.94±2.39	180.00
PUT-L	74.77±17.67	80.10±14.94	84.66±9.72	86.55±2.42	90.00
PUT-R	74.80±17.78	78.84±15.10	85.90±9.28	85.51±2.57	90.00
THA-L	3.31±35.86	4.40±24.97	3.44±19.24	5.50±2.35	10.00
THA-R	2.48±30.50	3.36±19.63	2.67±14.17	5.11±2.36	10.00
WM	-7.43±14.35	-5.95±12.33	-5.44±7.31	-2.59±1.66	0.00
RN-L	95.66±36.19	129.41±22.95	133.49±10.63	131.22±2.32	130.00
RN-R	95.96±44.40	126.67±22.72	135.58±11.81	129.79±2.51	130.00
SN-L	158.49±32.41	151.66±24.95	158.15±11.43	159.16±3.98	160.00
SN-R	139.56±30.15	144.07±22.01	154.88±9.65	159.43±4.71	160.00
CC-L	-30.85±23.38	-28.67±17.24	-36.24±10.14	-31.28±2.45	-30.00
CC-R	-32.08±24.01	-26.41±18.83	-37.56±10.39	-30.50±2.36	-30.00
CSF	-20.74±19.21	-17.81±13.12	-33.31±11.31	-15.40±2.25	-14.00
SSV	420.43±61.28	447.76±23.11	442.70±12.95	450.83±2.52	450.00
V	369.52±85.28	408.74±58.89	446.65±48.29	446.90±4.33	450.00
CMB1	3604.8±709.84	2784.73±772.89	958.42±37.07	2992.54±2.68	3000.00
CMB2	837.13±97.45	922.31±83.85	990.91±12.36	995.58±1.26	1000.00
CaD1	-855.56±98.61	-970.63±85.75	-995.38±17.41	-1002.92±1.42	-1000.00
CaD2	-3617.62±715.04	-3914.88±770.67	-1084.43±8.72	-3002.70±2.30	-3000.00
PG	-3605.53±692.29	-3885.88±760.06	-1053.80±47.14	-2998.92±1.97	-3000.00

CN (Caudate Nucleus), GP (Globus Pallidus), PUT (Putamen), THA (Thalamus), WM (White Matter), RN (Red Nucleus), SN (Substantia Nigra), CC (Crus Cerebri), CSF (Cerebrospinal Fluid), SSV (Straight Sinus Vein), V (mean of all Veins), CMB (Cerebral Micro Bleed), CaD (Calcium Deposit), PG (Pineal Gland), L (Left), R (Right), and ppb (parts per billion) unit.

4.2   In Vivo Data

In this section, results for both *in vivo* test datasets are shown.

4.2.1   Single Case with Multiple Orientations

Based on the L-curve analysis using the single high resolution human *in vivo* data (discussed in Section 3.4.1) and by assuming $\lambda_1 = 0.005\lambda_2$ for the purpose of bringing the two regularization terms to the same scale, $\lambda_2 = \{1, 1.47, 1.00, 1.00\} \times 10^{-4}$ provided the best results in terms of residual errors for FA_LTE_1, FA_HTE_1, FA_LTE_2, and FA_HTE_2, respectively (see Figure 4.1D-F). The structural terms used in the scSWIM cost function are illustrated in Figure 4.3. Specifically, Figure 4.3A-D show the edge and structural matrices P (includes P_x, P_y, and P_z) and R. The binary matrix P excludes the extracted edges from the enhanced T1-weighted and initial susceptibility while the binary mask R excludes the deep gray matter structures, vessels, and other high susceptibility regions (the complement of P and R masks are shown in the figure for better visualization). Figure 4.3E-H shows the conventional T1-weighted (Figure 4.3E) and T1WE (Figure 4.3H) from STAGE and their corresponding extracted edges (final P representation of extracted edges in three directions). It can be seen visually that the contrast between grey matter and white matter of the T1WE is higher than the conventional T1W image and its corresponding edge matrix, P_{T1WE}, provides more information about the edge.
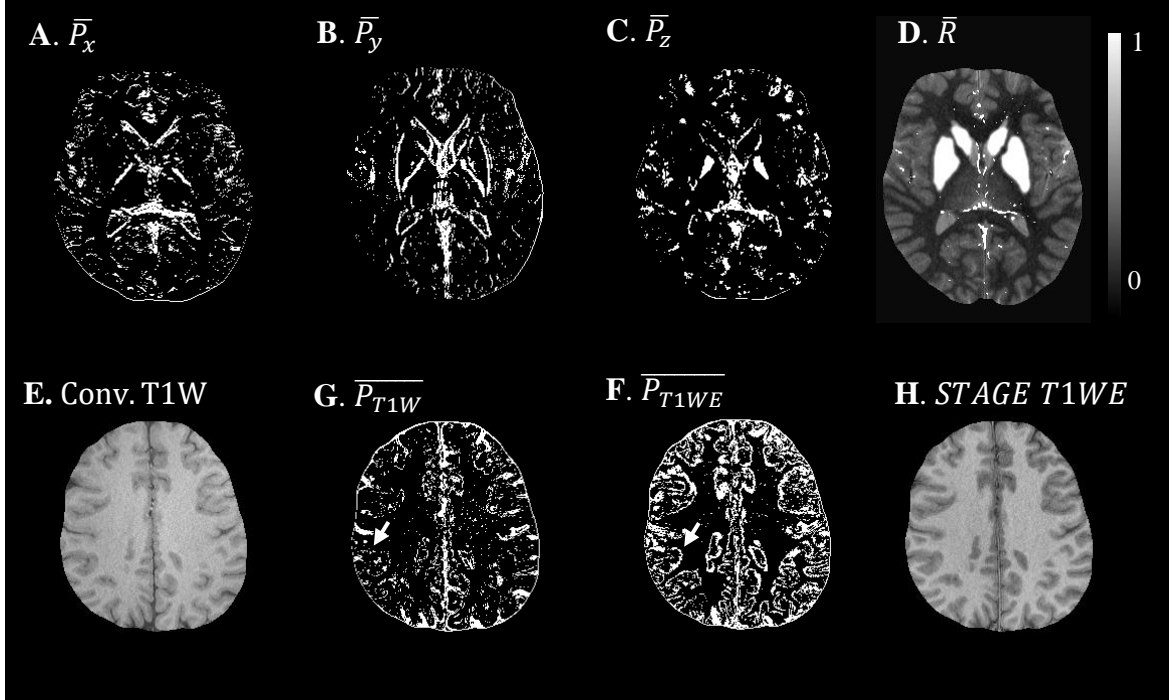
Figure 4.3. Illustration of scSWIM constraints and comparison of constraints extracted from conventional T1W and STAGE T1WE for the single high-resolution *in vivo* data. The first row shows the complement of the scSWIM structural constraints for the single high-resolution *in vivo* data: complement of edge matrix, $\bar{P}$, in the x, y, and z directions (**A-C**), and the : complement of structural matrix, $\bar{R}$ (**D**). The second row shows the advantage of extracting the constraints from STAGE versus conventional GRE data: conventional T1W (**G**), STAGE T1WE (**H**), and the complement of the extracted edges (product of three directions) from conventional T1W (**F**) and STAGE T1WE (**G**). As seen, (**G**) provides more information about the white and gray matter edges (white arrow) and is less noisy than (**F**).

Figure 4.4 shows three orthogonal views of the reconstructed multi-echo, multi-flip angle susceptibility images for this high-resolution human data set using the TKD (Figure 4.4A-C), iSWIM (Figure 4.4D-F), MEDI (Figure 4.4G-I), scSWIM (Figure 4.4J-L), and COSMOS (Figure 4.4M-O) methods. It can be seen in these images that scSWIM has less

noise while the sharpness of the vessels and other brain structures are well-preserved. MEDI also provides a smooth reconstruction, but in the regions that are close to the veins, there are still some remaining artifacts.
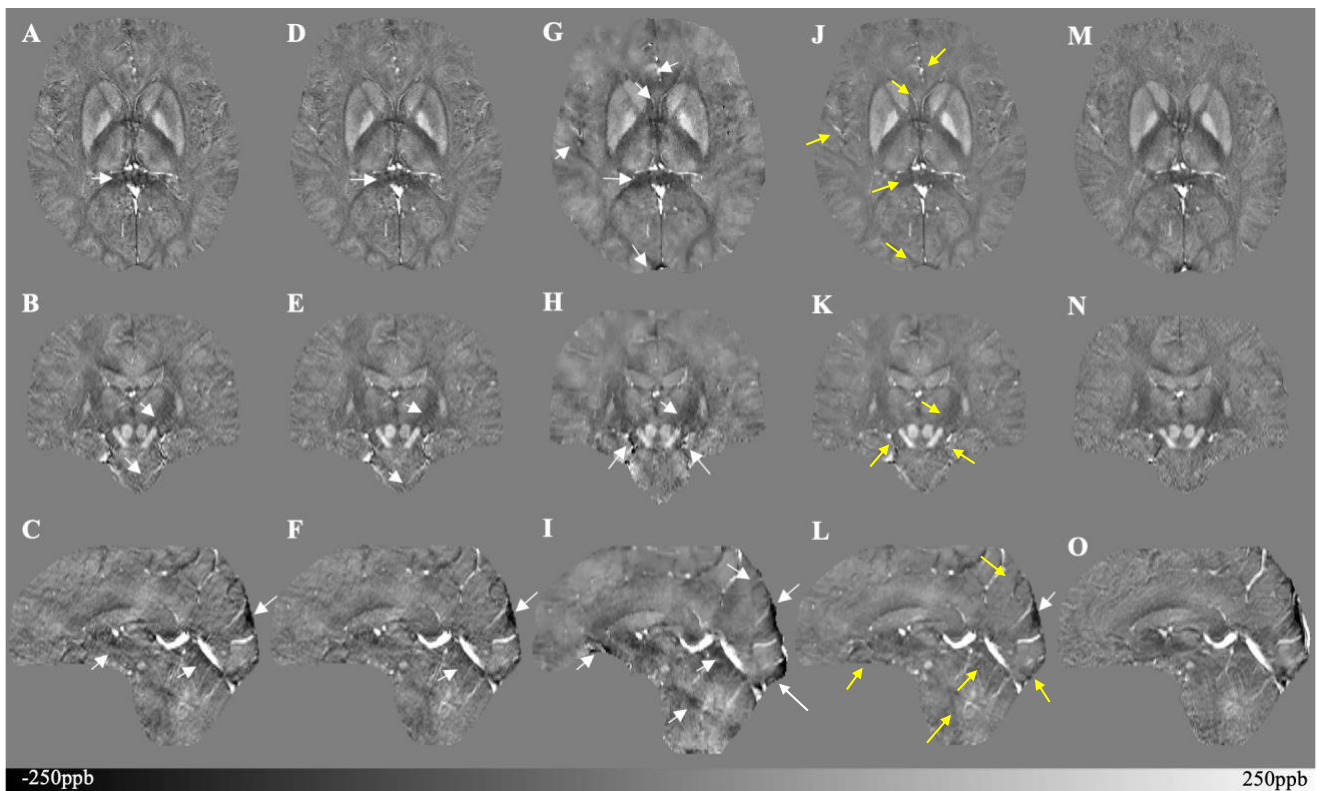
Figure 4.4. Depiction of multi-echo, multi-flip angle QSM images using different methods for the single high-resolution *in vivo* data. This figure shows three orthogonal views of the reconstructed multi-echo, multi-flip angle susceptibility maps from TKD (**A-C**), iSWIM (**D-F**), MEDI (**G-I**), scSWIM (**J-L**), and COSMOS (**M-O**) for the single high-resolution *in vivo* data. All of the images are displayed with the same window/level settings. White arrows show streaking artifacts while yellow arrows show the reduction of these artifacts in scSWIM. The SNR and image quality are best in the scSWIM images, while the sharpness of the vessels and other brain structures are preserved.

The measured susceptibility values in different structures are summarized in Table 4.2.

Table 4.2 Measured susceptibility values (mean ± standard deviation) in ppb for different structures in the reconstructed QSM images using TKD, iSWIM, MEDI, scSWIM, and COSMOS methods for the multi-echo, multi-flip angle in the single high-resolution *in vivo* data. The susceptibilities for the left and right CN, PUT, GP, RN, and SN were measured.

Regions	TKD	iSWIM	MEDI	scSWIM	COSMOS
CN-L	39.54±29.34	39.13±29.66	53.52±33.58	50.63±26.11	37.5±34.1
CN-R	39.87±29.36	38.11±29.32	47.85±28.98	51.95±24.38	38.2±32.5
GP-L	90.22±48.18	98.32±53.86	120.52±59.17	125.28±53.14	115.3±66.3
GP-R	90.67±42.59	98.92±48.95	115.29±43.19	123.89±45.48	111.3±55.0
PUT-L	30.19±32.36	29.58±33.22	43.10±35.50	50.24±27.44	42.0±32.0
PUT-R	29.37±32.43	29.31±33.08	33.89±34.56	47.45±30.06	36.43±32.95
THA-L	5.85±32.00	2.82±28.89	3.34±39.32	6.72±25.29	-1.89±38.25
THA-R	7.47±32.31	2.92±30.28	7.16±37.38	8.84±25.41	-2.49±38.77
RN-L	66.04±28.71	66.63±32.08	84.80±35.88	99.46±34.00	91.04±48.14
RN-R	101.68±35.38	113.07±43.18	114.85±39.88	120.85±39.22	95.18±53.17
SN-L	114.78±67.60	129.69±72.71	124.34±78.56	140.86±73.14	129.00±81.30
SN-R	111.97±58.00	124.66±69.93	127.47±69.16	147.67±69.67	144.25±79.86
DN-L	83.69±36.22	86.79±42.45	82.11±36.57	93.37±38.73	95.39±44.07
DN-R	74.97±35.69	82.21±40.28	63.23±39.63	92.17±38.63	84.70±47.20
SSV	424.62±43.73	422.32±43.65	395.39±50.01	411.93±42.46	404.95±38.53
ICV	281.52±59.40	298.13±54.02	302.49±54.77	326.07±53.94	316.82±67.50
CSF	16.96±28.67	20.83±26.19	26.65±25.56	28.40±22.33	18.54±43.16
WM	9.67±15.88	9.74±15.48	13.12±11.14	10.46±9.71	1.06±18.13

CN (Caudate Nucleus), GP (Globus Pallidus), PUT (Putamen), THA (Thalamus), RN (Red Nucleus), SN (Substantia Nigra), DN (Dentate Nucleus), SSV (Straight Sinus Vein), ICV (Internal Cerebral Vein), CSF (Cerebrospinal Fluid), WM (White Matter), L (Left), R (Right), and ppb (parts per billion) unit.
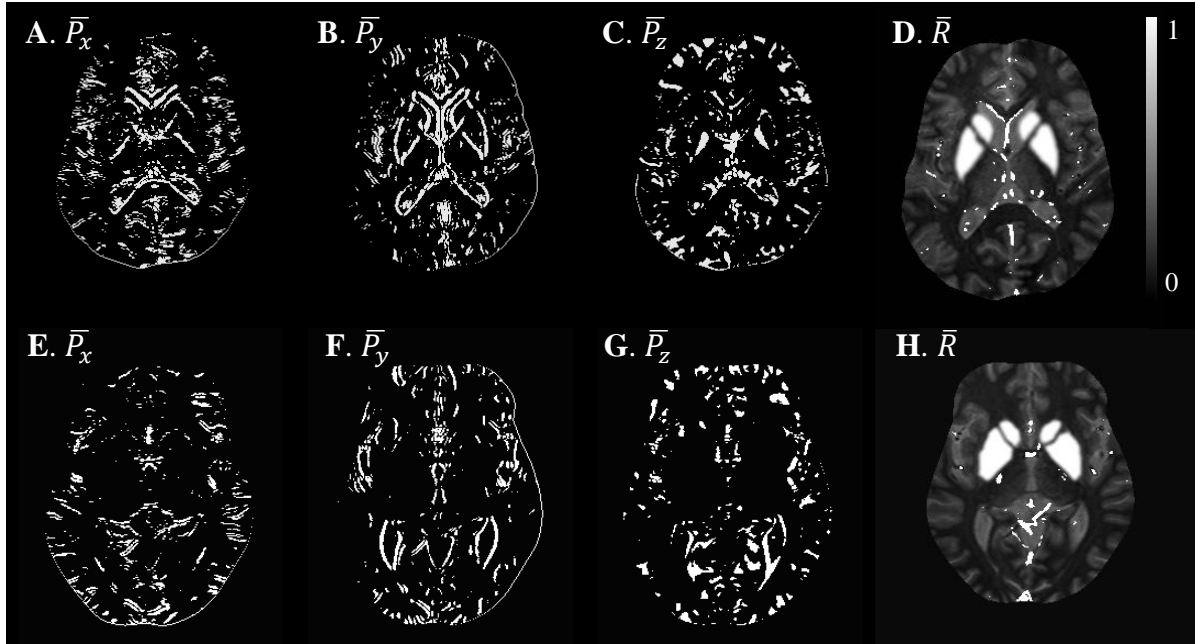
Figure 4.5. Illustration of scSWIM structural constraints for a selected 54-year old case from each of the PD (**A-D**) and HC (**E-H**) groups from the low-resolution STAGE dataset. The complement of the scSWIM structural constraints, edge matrix, $\bar{P}$, in the x, y, and z, and structural matrix, $\bar{R}$, are shown.

4.2.2 Healthy Controls versus Parkinson's Disease Patients

In Figure 4.5, the structural terms used in the scSWIM cost function for one selected case from each of the PD (Figure 4.5.A-D) and HC (Figure 4.5.E-H) groups with lower resolution data (discussed in Section 3.4.2) are illustrated. Here it can be seen that the edges are still well preserved with this in vivo STAGE approach. Figure 4.6 shows the reconstructed multi-echo, multi-flip angle susceptibility images using TKD (Figure 4.6.A,E), iSWIM (Figure 4.6.B,F), MEDI (Figure 4.6.C,G), and scSWIM (Figure 4.6.D,H) methods for the same two examples of this data. There are artifacts around the basal ganglia structures and larger veins in the TKD, iSWIM and MEDI (shown with white

arrows). Furthermore, for the HC case that is shown in the second row (Figure 4.6.E-H), the PG looks dilated in MEDI compared to the other methods (marked by a red arrow) and there appear to be some ringing artifacts and dark bands as well (green and yellow arrows, respectively). These dark bands might be interpreted as real structures when in fact they are not really present.
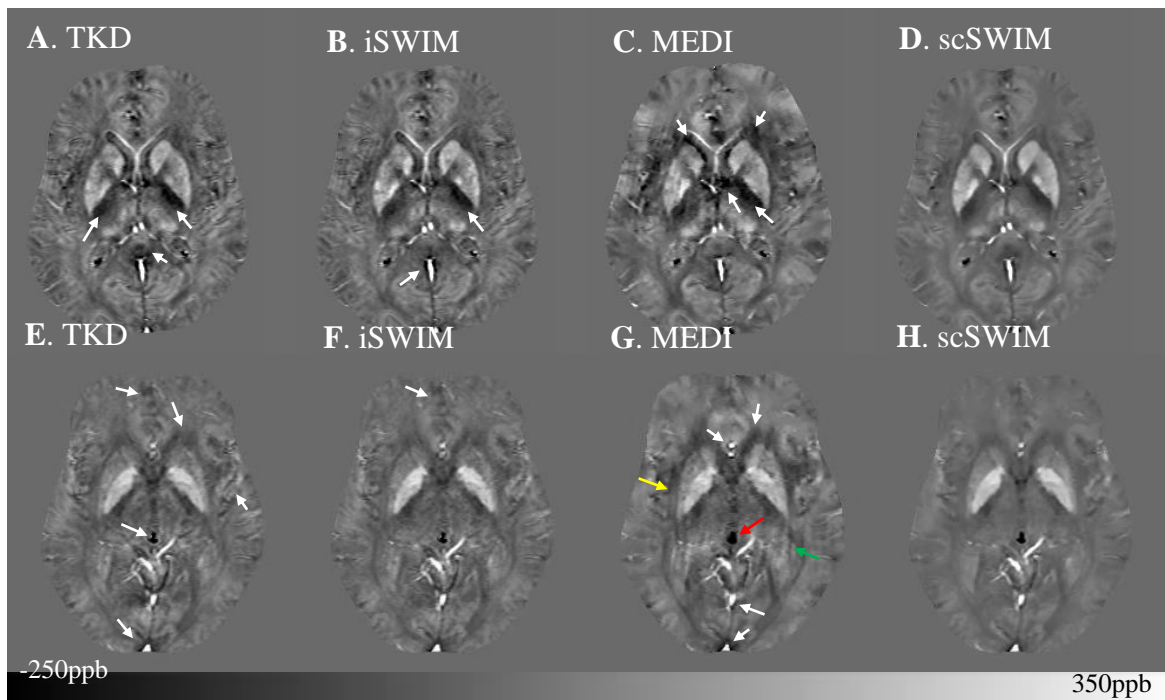
Figure 4.6. Depiction of multi-echo, multi-flip angle QSM images using different methods for the one selected case from PD (**A-D**) and HC (**E-H**) groups from the low-resolution dataset. Multi-echo, multi-flip angle susceptibility maps from TKD (**A,E**), iSWIM (**B,F**), MEDI ($\lambda = 350$) (**C,G**), and scSWIM (**D,H**) are shown for the two healthy subjects from Figure 4.5. The artifacts around the basal ganglia and larger veins in the TKD, iSWIM, and MEDI are shown by the white arrows. In the second row (**E-H**), the pineal gland looks dilated in MEDI compared to other methods (red arrow).

Table 4.3 Averaged susceptibility values (mean ± standard deviation) in ppb for midbrain structures in the reconstructed QSM images using TKD, iSWIM, MEDI, and scSWIM for ten healthy controls (HC) and ten Parkinson's Disease (PD) patients from the low-resolution in vivo STAGE dataset from a Siemens 3T PRISMA scanner. Also, the results from [15] are summarized in the last column, where the DGM structures are measured in both hemispheres in 24 healthy subjects from a GE 3T scanner.

Regions	HC/PD	TKD	iSWIM	MEDI	scSWIM	Measurements from [15]
CN-L	HC	41.68±7.33	41.7±7.98	51.37±9.95	49.4±6.88	52.4±7.6
	PD	52.77±8.99	54.88±10.02	53.29±7.67	54.35±8.2	54.7±6.9
CN-R	HC	49.07±6.04	46.98±6.02	54.33±8.73	52.76±5.91	54.6±6.6
	PD	49.88±9.08	51.69±9.81	46.19±9.9	52.73±8.36	59.3±6.7
GP-L	HC	106±16.26	117.88±18.92	118.36±19.85	130.7±18.76	127.8±7.8
	PD	111.49±8.8	125.02±10.17	130.27±13.33	136.98±10.08	127.6±9.9
GP-R	HC	112.22±18.48	123.44±21.17	128.22±18.43	134.57±20.52	133.1±10.1
	PD	104.24±11.34	116.05±12.58	126.77±14.49	127.17±11.45	133.7±10.0
PUT-L	HC	60.37±8.53	63.26±9.63	60.67±10.12	73.58±11.06	72.8±7
	PD	57.87±5.75	60.78±6.89	61.68±8.45	68.91±7.24	73.6±7.8
PUT-R	HC	53.46±10.41	55.75±11.26	53.64±12.87	64.9±12.35	68.7±6.4
	PD	52.87±6.41	55.56±7.49	54.61±8.53	63.16±7.65	75.8±6.6
RN-L	HC	86.41±18.33	93.49±20.08	102.61±19.82	105.21±19.24	102.9±12.9
	PD	95.37±17.42	107.71±19.76	94.64±10.16	108.1±15.67	112.2±13.8
RN-R	HC	85.57±20.17	93.1±22.71	85.74±28.1	100.15±22.5	108.1±13.0
	PD	102.19±16.98	113.46±18.04	95.99±23.76	112.6±17.92	112.8±13.1
SN-L	HC	101.93±24.77	113.77±28.11	116.97±29.05	124.46±25.63	127.5±10.8
	PD	120.23±19.41	134.69±21.67	129.69±25.36	144.14±18.94	147.5±10.5
SN-R	HC	93.24±39.28	103.21±45.26	103.06±45.67	112.2±42.33	115.4±11.6
	PD	111.87±28.26	125.31±32.81	125.5±33.84	131.33±29.14	139.8±10.4

CN (Caudate Nucleus), GP (Globus Pallidus), PUT (Putamen), RN (Red Nucleus), SN (Substantia Nigra), L (Left), R (Right), and ppb (parts per billion) unit.

Table 4.3 summarizes the averaged measured susceptibility values (mean ± standard deviation) in the reconstructed QSM images from the four different methods for the 10 PD and 10 HC subjects. The last column of this table states the results from [15] where the

DGM structures are measured in both hemispheres in 25 PD and 24 HC subjects from a GE 3T scanner. As seen from the table, scSWIM measurements in the basal ganglia are in good agreement with the literature.

Figure 4.7 shows the correlation between the zero-referenced estimated susceptibility for deep gray matter structures from different reconstruction methods with the actual susceptibility from the numerical model for the simulated data and reconstructed COSMOS for the *in vivo* data. The measured susceptibility value for the CSF in each method is used
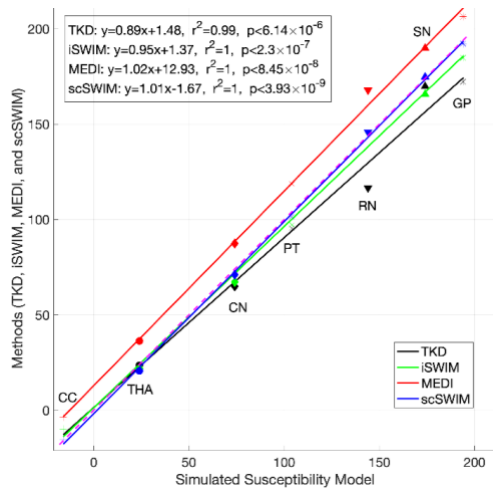
A. Simulated Data **B**. *In Vivo* Data

Figure 4.7. This figure shows the correlation of the susceptibilities of different basal ganglia structures (bilateral, that is, the average of left and right) in the reference image with the ones in the reconstructed images using different methods in the simulated data (**A**) and *in vivo* data (**B**) (TKD (black), iSWIM (green), MEDI (red), and scSWIM (blue)). All methods correlated well with iron content, but scSWIM provided the best result relative to the correct absolute susceptibility. The dashed pink line corresponds to the line of identity between the individual reconstruction method and the reference susceptibility model and COSMOS for simulated and *in vivo* data, respectively.

To zero-reference the measurements. Among these methods, scSWIM (in blue color) has the closest values to the reference image in both datasets. The slope of scSWIM is 1.01(0.99) while TKD, iSWIM and MEDI are 0.89(0.78), 0.95(0.90), and 1.02(0.89) for simulated (and *in vivo*) data, respectively. The correlation coefficients in all methods are close to one and p-values are less than 0.001.

Also, Figure 4.8 shows the correlation between the estimated susceptibility for deep gray matter structures from scSWIM with the measurements reported in [15] for both HC and PD cases. In both these cases, scSWIM is in good agreement with the values in [15] where the slope for HC (and PD) is 1.02 (1.03).

A. HC   **B**. *PD*

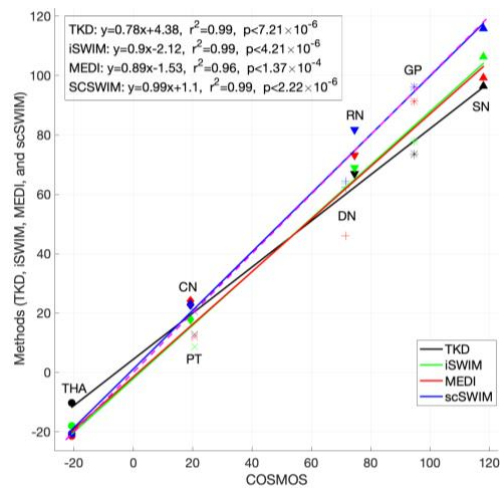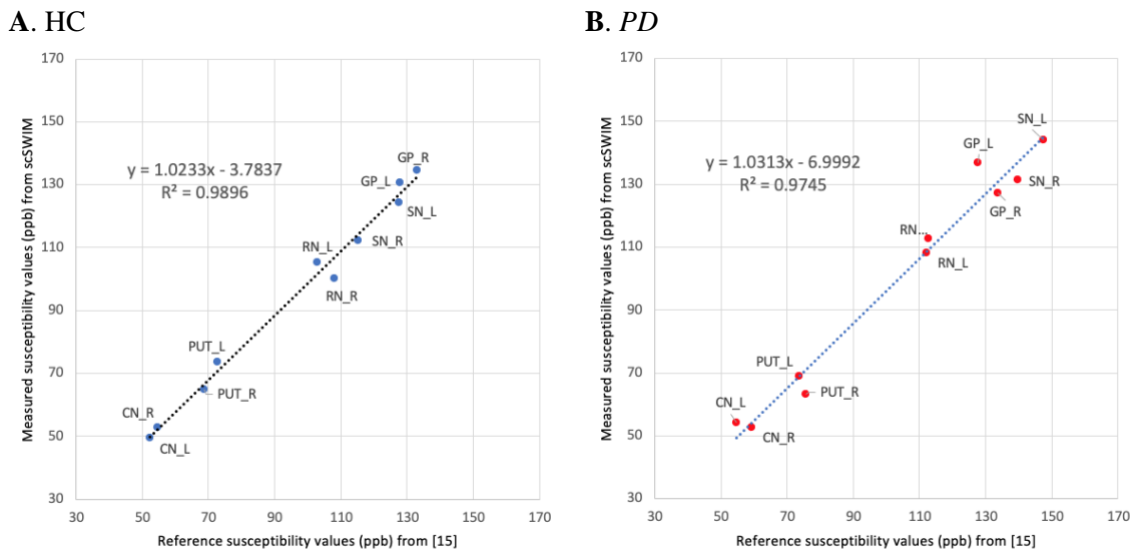**Figure 4.8.** This figure shows the correlation of the susceptibilities of different basal ganglia structures from the reference values reported in [15] with the ones in the reconstructed image using scSWIM method for the HC (**A**) and *PD* (**B**) cohorts. In both these cohorts, scSWIM is in good agreement with the reported values in [15].

4.3 scSWIM Computation Time

The current implementation of scSWIM for a single echo converges in 3 and 5 iterations for the simulated and *in vivo* data, respectively. Each iteration consists of a minimization process that uses a preconditioned conjugate gradient solver. For our zero-padded in vivo data with a matrix size of $512 \times 512 \times 128$, the total processing time for each single-echo scSWIM is currently 2~5 depending on the number of iterations using a Windows 10, Intel CPU i7-3770 with 4 cores and 16GB RAM.

5 Discussion

The quantitative and qualitative analysis on both simulated data and human *in vivo* data showed that the reconstructed TKD suffers from streaking artifacts and underestimates the susceptibility values of deep gray matter and veins. The streaking artifact is reduced in iSWIM by using constraints from high susceptibility structures, but the final image is still noisy in the homogeneous regions. Thanks to the use of an ℓ_1-norm regularization MEDI creates high SNR results. However, some streaking artifacts remain in regions where magnitude data were inconsistent with the susceptibility map. On the other hand, scSWIM used both ℓ_1 and ℓ_2 regularization terms to protect edges and structures while also allowing smoothing to increase SNR in regions without structure, and it successfully reduced streaking artifacts leading to less noise and faithful estimates of the susceptibility. Furthermore, scSWIM outperformed the other methods in reconstructing the susceptibility map in the presence of CMBs and CaDs with high susceptibilities. In simulated data, both microbleeds with susceptibilities of 1000 ppb and 3000 ppb and calcium objects with susceptibilities of -1000 ppb and -3000 ppb were reconstructed accurately using scSWIM compared to other methods. Also, in scSWIM, the standard deviation of the measured susceptibilities (Table 4.1) in all structures even in the CMB or CaD with the highest susceptibility values was much lower than other methods showing the strengths of this

multi-echo approach. Although MEDI provides a smooth QSM image under normal circumstances, it appears to have trouble in reconstructing the data in the presence of high susceptibilities such as seen with the CMB and CaD in the simulated model and for the pineal gland in the *in vivo* data (which appeared dilated compared to that in scSWIM). This could be due to the fact that MEDI uses phase fitting across multiple echoes, and high susceptibilities can cause both signal loss at the edge of the object and severe aliasing at longer echoes. Furthermore, in the *in vivo* data, one could observe slight streaking with MEDI around the large veins that could be due to the inconsistency between the magnitude and susceptibility data.

The *in vivo* results for scSWIM showed average susceptibilities for the ten PD and ten HC cases very close to the reported values in the literature [15]. Also, the measured susceptibilities in the reconstructed COSMOS (Table 4.2) were not as close to scSWIM and MEDI as one would have hoped because it likely contained errors due to registration of the different orientation data and noise in the data. The registration error was higher and more noticeable in the regions near the surface of the brain. Luckily, most of the regions of interest (the deep gray matter) in this paper are near the core of the brain where the registration error is smaller; therefore, this central region can still be used as a baseline to compare the different methods.

5.1 Structural Constraints in scSWIM

The cost function of scSWIM includes two regularization terms. The ℓ_1-norm regularization term which is based on a P mask to penalize the noisy non-edge pixels and the ℓ_2-norm regularization term which is based on the R mask that prevents smoothing in the excluded high susceptibility regions. If the pre-processing fails to extract the edges of a true structure, then the P mask will penalize and smooth them. On the other hand, if R fails to exclude a high susceptibility structure, the streaking artifacts from this structure will remain and its mean susceptibility will be reduced due to smoothing. This is because the R mask protects the structures of high susceptibility from being over smoothed by the ℓ_1-norm regularization term. The overall performance of the cost function works well when the edges and structures are best defined.

5.2 Optimal Parameter Selection for scSWIM

In the regularization-based approaches, there is always a trade-off between obtaining accurate susceptibility values, reducing streaking artifacts, and increasing SNR. Figure 5.1 shows the effect of scSWIM parameters, λ_1 and λ_2, on the reconstructed QSM image. As seen in Figure 5.1A-B, λ_1 controls the spatial smoothness by applying the sparsity constraint on the gradient of the susceptibility map. The larger the λ_1, the smoother the non-edge regions will be for both the background and basal ganglia (basically increasing the SNR). On the other hand, λ_2 also controls smoothing the background but protects the

objects defined by the R mask. Smaller λ_2 reduces the effect of the regularization term and increases the effect of the data fidelity term and the streaking artifacts will not be handled as well (see Figure 5.1D). On the other hand, larger λ_2 will increase the effect of the regularization term and reduce the effect of the data fidelity term and will result in an over-smoothed image where the background such as WM and GM and smaller objects would be washed out (see Figure 5.1E).

Therefore, the challenging part of scSWIM is to find the optimal parameters to keep sharp edges, smooth where appropriate, and satisfy the data fidelity condition. However, finding optimal values for more than one parameter in regularization problems is still a difficult problem.

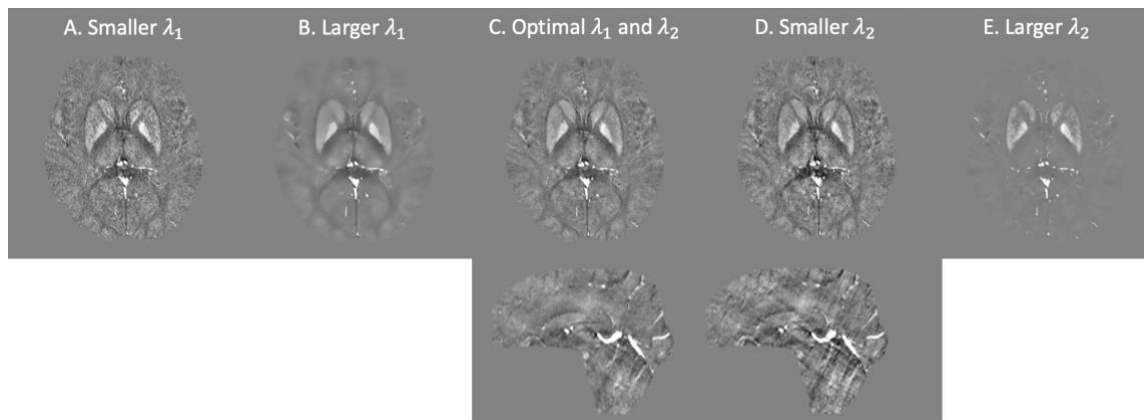**Figure 5.1.** Effect of λ_1 and λ_2 parameters on the reconstructed QSM using scSWIM method. The λ_1 parameter controls the spatial smoothness (A and B) and λ_2 controls smoothing of the background regions excluding the high susceptibility regions (D and E). The second row for (C) and (D) illustrates the sagittal view showing the streaking artifact when using smaller λ_1 values.

With the admission of sub-optimality, we assumed that the ratio of λ_1 and λ_2 is fixed. For this purpose, we compared the P and R masks and also the first and second regularization terms and observed that $\lambda_1 = 0.005\lambda_2$ brought the two terms to the same order. The final step was to determine the optimal value for λ_2. This was accomplished using the L-curve approach that plots the residual data fidelity versus the regularization for different regularization parameters and selecting the value that results in the maximum curvature. For multi-echo, multi-flip angle scSWIM, the L-curves were analyzed for each individual scan separately and the optimal λ_2 values selected accordingly.

5.3 Multi-Echo, Multi-Flip Angle scSWIM

As mentioned before, STAGE imaging uses double-flip angle, double-echo GRE scans. The multi-echo, multi-flip angle scSWIM or STAGE scSWIM is generated by an R_2^*-based weighted averaging of the individual echo scSWIM data sets. Besides having higher SNR in the STAGE scSWIM results, each individual scSWIM dataset can be reviewed separately if desired. It would be of interest to compare the QSM results with those from the R2* maps or even the T1maps given that iron can affect the T1 of tissue. Recently, there has been more interest in multi-contrast quantitative mapping in diseases such as Parkinson's disease and dementia where a more systemic quantitative approach is being taken with 3D data. Iron has played a key role in these studies not just in the basal ganglia but also in the hippocampus and motor cortex and cortical gray matter in general.

More importantly, the final STAGE scSWIM will keep regions that have been removed by the phase quality control map at longer echo times (see Figure 5.2). An alternate approach would be reconstructing QSM from the linear fit to the phase as done in MEDI. However, regions of high susceptibility phase aliasing can be severe, and phase fitting may not be successful. Furthermore, severe loss of signal in and around the object (blooming artifacts) will occur for high susceptibilities that will result in a significantly under-estimated susceptibility. The use of shorter echo times and the weighting factors can favor the short echo data replacing the long echo data when the susceptibilities are very high as in the case of the CMBs and CaD as shown in the results section and near the air/tissue interfaces.
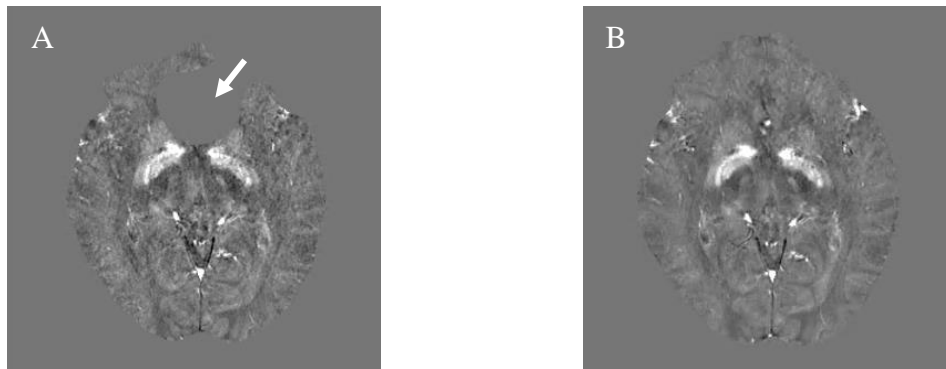
Figure 5.2. The region that has been removed by the phase quality control map at longer echo, TE=18.5ms, at a single-echo QSM (A) is kept in the multi-echo multi-filp angle STAGE scSWIM (B) using the shorter echo data.

STAGE uses the conventional SWI with two flip angles and is effectively available at any site that can run 3D GRE imaging. It is a 5-minute scan (2.5 minutes for each flip angle) that provides eight qualitative and seven quantitative clinically useful images such as T1maps, spin density maps, QSM, R2*, B1 field corrections and etc. Although the high-resolution STAGE scan time using 0.67mm×0.67mm×1.34mm takes a longer time to collect (~10 minutes), using a compressed sense factor of 3 to 4 the scan times can be brought back to a time frame of 7 to 5 minutes, respectively. The proposed scSWIM method achieved the best results when processing double-echo, double-flip angle STAGE data by using the derived T1WE images to extract reliable geometry constraints, but it can also be performed on a single-echo T1W SWI dataset.

6   Conclusions and Future Directions

6.1   Conclusions

In this thesis, we have proposed a constraint-based algorithm called scSWIM to reconstruct the susceptibility map from multiple flip angle, multiple echo STAGE data. scSWIM uses the structural information from both magnitude data and susceptibility map in a single step. It specifically takes advantage of the enhanced contrast available in STAGE imaging to define prior information about the edges of the white matter and gray matter.

scSWIM is tested on both simulated and *in vivo* human brain data and results show that streaking artifacts are suppressed, and SNR is increased. Further, the measured susceptibilities are accurate relative to the brain model used, and scSWIM works well even for regions with high susceptibility such as microbleeds and calcifications.

This study shows that using a data fidelity term and structural constraints results in reduced noise and streaking artifacts while preserving structural details. Furthermore, the use of STAGE imaging with multi-echo and multi-flip data helps to improve the signal-to-noise ratio in QSM data and yields less artifacts.

6.2   Future Directions

As mentioned in Section 2.5.3, the acquired phase data includes both the local field from the brain and the induced background field from outside the brain. To be able to reconstruct QSM of the brain, the background field needs to be removed. However, this step either erodes the edges of the brain or generates inaccurate field maps around the edges. In conditions like traumatic brain injury (TBI) or subarachnoid hemorrhage (SAH) where the bleeding can occur at the edge of the brain, the background field removal step is undesired. Therefore, we aim to generalize scSWIM to be applied directly to the total field and skip the background field removal preprocessing step. For this purpose, two steps of scSWIM could be used. The first step would be to use the structural constraints derived from the outline of the brain to separate the brain/skull from the outside air. This would provide an estimate of the susceptibility distribution that comes from the presence of the brain in air. Then, the field from these sources would be simulated using the forward filter mentioned in Equation (2.11). In the next step, the local field of the brain would be generated by subtracting the simulated field from the total field. Finally, the second scSWIM would be run on the local field using the constraints proposed in this thesis. This way, the background field removal step is skipped without the need for erosion at the edge of the brain. We already tested this method on the simulated brain model and achieved promising preliminary results. Our next step will be to evaluate it on the *in vivo* test dataset.

Furthermore, as discussed in Section 2.4, QSM does not reflect the absolute susceptibility values, and it is only able to quantify the magnetic susceptibility with respect

to a reference value. Therefore, to compare different subjects and stages of the disease, a proper reference tissue and baseline value is needed to get the absolute susceptibility from the QSM. In literature, different tissues are used for zero-referencing, such as white matter and CSF [60,61]. On the other hand, the quantitative R2* map that is generated from the multi-echo GRE scan is a robust imaging technique that provides absolute values. Therefore, no normalization is needed. Different studies investigated the linear correlation of R2* and QSM with iron concentration in different brain structures, shown there is a strong correlation between them [62]. Therefore, considering this correlation, one possibility is to calculate the QSM reference value using the R2* of white matter to set baseline. This provides an automatic way to zero-reference the QSM values.

Bibliography

[1]   J. Reichenbach, R. Venkatesan, D. Schillinger, D. K. Kido, and E. M. Haacke, "Small vessels in the human brain: MR venography with deoxyhemoglobin as an intrinsic contrast agent," *Radiology*, vol. 204, pp. 272–77, 1997.

[2]   E. M. Haacke *et al.*, "Imaging iron stores in the brain using magnetic resonance imaging," *Magn. Reson. Imaging*, vol. 23, no. 1, pp. 1–25, 2005.

[3]   E. M. Haacke, Y. Xu, Y. C. N. Cheng, and J. R. Reichenbach, "Susceptibility weighted imaging (SWI)," *Magn. Reson. Med.*, vol. 52, no. 3, pp. 612–618, 2004.

[4]   R. Salomir, B. D. De Senneville, and C. T. W. Moonen, "A fast calculation method for magnetic field inhomogeneity due to an arbitrary distribution of bulk susceptibility," *Concepts Magn. Reson. Part B Magn. Reson. Eng.*, vol. 19, no. 1, pp. 26–34, 2003.

[5]   J. Neelavalli, Y.-C. N. Cheng, and M. E. Haacke, "Method for Susceptibility Calculation in Multiple Source Object Distribution with Arbitrary Susceptibilities : A Preliminary Report," in *Proc. Intl. Soc. Mag. Reson. Med.*, 2005, vol. 13, p. 2333.

[6]   E. M. Haacke, S. Mittal, Z. Wu, J. Neelavalli, and Y. C. N. Cheng, "Susceptibility-weighted imaging: Technical aspects and clinical applications, part 1," *Am. J. Neuroradiol.*, vol. 30, no. 1, pp. 19–30, 2009.

[7]   S. Mittal, Z. Wu, J. Neelavalli, and E. M. Haacke, "Susceptibility-weighted imaging: Technical aspects and clinical applications, part 2," *Am. J. Neuroradiol.*, vol. 30, no. 2, pp. 232–252, 2009.

[8]   E. M. Haacke, S. Liu, S. Buch, W. Zheng, D. Wu, and Y. Ye, "Quantitative susceptibility mapping: Current status and future directions," *Magn. Reson. Imaging*, vol. 33, no. 1, pp. 1–25, 2015.

[9]   B. Bilgic, A. Pfefferbaum, T. Rohl, E. V Sullivan, and E. Adalsteinsson, "MRI estimates of brain iron concentration in normal aging using quantitative susceptibility mapping," *Neuroimage*, vol. 59, pp. 2625–2635, 2012.

[10]   W. Chen *et al.*, "intracranial calcifications and hemorrhages: Characterization with Quantitative Susceptibility Mapping," *Radiology*, vol. 270, no. 2, 2014.

[11]   A. Deistung *et al.*, "Quantitative Susceptibility Mapping Differentiates between Blood Depositions and Calcifications in Patients with Glioblastoma," *PLoS One*, vol. 8, no. 3, pp. 1–8, 2013.

[12]   E. M. Haacke, J. Tang, J. Neelavalli, and Y. C. N. Cheng, "Susceptibility Mapping

as a Means to Visualize Veins and Quantify Oxygen Saturation," *J Magn Reson Imaging*, vol. 32, no. 3, pp. 663–676, 2010.

[13] C. Langkammer *et al.*, "Quantitative susceptibility mapping in multiple sclerosis," *Radiology*, vol. 267, no. 2, pp. 551–559, 2013.

[14] K. Ghassaban, S. Liu, C. Jiang, and E. M. Haacke, "Quantifying iron content in magnetic resonance imaging," *Neuroimage*, vol. 187, pp. 77–92, 2019.

[15] K. Ghassaban, N. He, S. K. Sethi, P. Huang, and S. Chen, "Regional High Iron in the Substantia Nigra Differentiates Parkinson ' s Disease Patients From Healthy Controls," *Front Aging Neurosci.*, vol. 11, p. 106, 2019.

[16] J. M. van Bergen *et al.*, "Quantitative susceptibility mapping suggests altered brain iron in premanifest Huntington's disease," *Physiol. Behav.*, vol. 37, no. 5, pp. 789–796, 2016.

[17] M. Vaas, A. Deistung, J. R. Reichenbach, A. Keller, A. Kipar, and J. Klohs, "Vascular and Tissue Changes of Magnetic Susceptibility in the Mouse Brain After Transient Cerebral Ischemia," *Transl. Stroke Res.*, vol. 9, no. 4, pp. 426–435, 2018.

[18] J. Wu *et al.*, "Cortical calcification in sturge-weber syndrome on MRI-SWI: Relation to brain perfusion status and seizure severity," *J. Magn. Reson. Imaging*, vol. 34, no. 4, pp. 791–798, 2011.

[19] K. M. Koch, T. B. Meier, R. Karr, A. S. Nencka, L. T. Muftuler, and M. McCrea, "Quantitative Susceptibility Mapping after Sport-related Concussion," *AJNR Am J Neuroradiol*, vol. 39, no. 7, pp. 1251–1221, 2018.

[20] S. Wharton, A. Schafer, and R. Bowtell, "Susceptibility Mapping in the Human Brain Using Threshold-Based k-Space Division," *Magn. Reson. Med.*, vol. 63, pp. 1292–1304, 2010.

[21] J. Tang, S. Liu, J. Neelavalli, Y. C. N. Cheng, S. Buch, and E. M. Haacke, "Improving Susceptibility Mapping Using a Threshold-Based K-space/Image Domain Iterative Reconstruction Approach," *Magn Reson Med.*, vol. 69, no. 5, pp. 1396–1407, 2013.

[22] C. Langkammer *et al.*, "Quantitative Susceptibility Mapping : Report From the 2016 Reconstruction Challenge," *Magn. Reson. Med.*, vol. 79, pp. 1661–1673, 2018.

[23] F. Schweser, K. Sommer, A. Deistung, and J. R. Reichenbach, "Quantitative susceptibility mapping for investigating subtle susceptibility variations in the human brain," *Neuroimage*, vol. 62, no. 3, pp. 2083–2100, 2012.

[24] L. Bao, X. Li, C. Cai, Z. Chen, and P. C. M. Van Zijl, "Quantitative Susceptibility Mapping Using Structural Feature Based Collaborative Reconstruction (SFCR) in the Human Brain," *IEEE Trans. Med. Imaging*, vol. 35, no. 9, pp. 2040–2050, 2016.

[25] T. Liu, P. Spincemaille, L. De Rochefort, B. Kressler, and Y. Wang, "Calculation of susceptibility through multiple orientation sampling (COSMOS): A method for conditioning the inverse problem from measured magnetic field map to susceptibility source image in MRI," *Magn. Reson. Med.*, vol. 61, no. 1, pp. 196–204, 2009.

[26] Y. Chen, S. Liu, Y. Wang, Y. Kang, and E. M. Haacke, "STrategically Acquired Gradient Echo (STAGE) imaging, part I: Creating enhanced T1 contrast and standardized susceptibility weighted imaging and quantitative susceptibility mapping," *Magn. Reson. Imaging*, vol. 46, no. July 2017, pp. 130–139, 2018.

[27] Y. Wang *et al.*, "STrategically Acquired Gradient Echo (STAGE) imaging, part II: Correcting for RF inhomogeneities in estimating T1 and proton density," *Magn. Reson. Imaging*, vol. 46, pp. 140–150, 2018.

[28] E. M. Haacke *et al.*, "STrategically Acquired Gradient Echo (STAGE) imaging, part III: Technical advances and clinical applications of a rapid multi-contrast multi-parametric brain imaging method," *Magn. Reson. Imaging*, vol. 65, pp. 15–26, 2020.

[29] S. Gharabaghi, S. Liu, Y. Wang, Y. Chen, T. Wischgoll, and E. M. Haacke, "Structurally Constrained Quantitative Susceptibility Mapping," in *27th Annual Meeting of ISMRM*, 2019.

[30] S. Gharabaghi *et al.*, "Multi-Echo Quantitative Susceptibility Mapping for Strategically Acquired Gradient Echo (STAGE) Imaging," *Front. Neurosci.*, vol. 14, p. 1070, 2020.

[31] R. W. Brown, Y. C. N. Cheng, E. M. Haacke, M. R. Thompson, and R. Venkatesan, *Magnetic Resonance Imaging: Physical Principles and Sequence Design*. Wiley-Blackwell, 2014.

[32] C. Liu, W. Li, K. A. Tong, K. W. Yeom, and S. Kuzminski, "Susceptibility-Weighted Imaging and Quantitative Susceptibility Mapping in the Brain Chunlei," *J Magn Reson Imaging*, vol. 42, no. 1, pp. 23–41, 2015.

[33] E. M. Haacke and J. R. Reichenbach, *Susceptibility Weighted Imaging in MRI: Basic Concepts and Clinical Applications*. Wiley Blackwell, 2011.

[34] S. M. Smith, "Fast robust automated brain extraction," *Hum. Brain Mapp.*, vol. 17, pp. 143–155, 2002.

[35] M. A. Schofield and Y. Zhu, "Fast phase unwrapping algorithm for interferometric applications," *Opt. Lett.*, vol. 28, no. 14, p. 1194, 2003.

[36] H. S. Abdul-Rahman, M. A. Gdeisat, D. R. Burton, M. J. Lalor, F. Lilley, and C. J. Moore, "Fast and robust three-dimensional best path phase unwrapping algorithm," *Appl. Opt.*, vol. 46, no. 26, pp. 6623–6635, Sep. 2007.

[37] W. Feng, J. Neelavalli, and E. M. Haacke, "Catalytic multiecho phase unwrapping scheme (CAMPUS) in multiecho gradient echo imaging: Removing phase wraps on a voxel-by-voxel basis," *Magn. Reson. Med.*, vol. 70, no. 1, pp. 117–126, 2013.

[38] Y. Chen, S. Liu, Y. Kang, and E. M. Haacke, "A rapid, robust multi-echo phase unwrapping method for quantitative susceptibility mapping (QSM) using strategically acquired gradient echo (STAGE) data acquisition," in *SPIE 10573, Medical Imaging 2018: Physics of Medical Imaging*, 2018.

[39] Y. Wang *et al.*, "Artery and vein separation using susceptibility-dependent phase in contrast-enhanced MRA," *J. Magn. Reson. Imaging*, vol. 12, no. 5, pp. 661–670, 2000.

[40] J. Neelavalli, S. Liu, Y.-C. N. Cheng, E. M. Haacke, and Z. Kou, "Effect of Orientation of 2D Phase High-Pass Filter on Susceptibility Mapping of Veins and Microbleeds," in *Proc Intl Soc Mag Reson Med 19 (2011)*, 2011, vol. 19, p. 4517.

[41] T. Liu *et al.*, "A novel background field removal method for MRI using projection onto dipole fields (PDF)," *NMR Biomed.*, vol. 24, no. 9, pp. 1129–1136, 2011.

[42] F. Schweser, A. Deistung, B. W. Lehr, and J. R. Reichenbach, "Quantitative imaging of intrinsic magnetic tissue properties using MRI signal phase: An approach to in vivo brain iron metabolism?," *Neuroimage*, vol. 54, pp. 2789–2807, 2011.

[43] S. Wharton, A. Schäfer, and R. Bowtell, "Susceptibility mapping in the human brain using threshold-based k-space division," *Magn. Reson. Med.*, vol. 63, no. 5, pp. 1292–1304, 2010.

[44] J. Liu *et al.*, "Morphology enabled dipole inversion for quantitative susceptibility mapping using structural consistency between the magnitude image and the susceptibility map," *Neuroimage*, vol. 59, no. 3, pp. 2560–2568, 2012.

[45] M. Jo and S. H. Oh, "A preliminary attempt to visualize nigrosome 1 in the substantia nigra for Parkinson's disease at 3T: An efficient susceptibility map-weighted imaging (SMWI) with quantitative susceptibility mapping using deep neural network (QSMnet)," *Med. Phys.*, vol. 47, no. 3, pp. 1151–1160, 2020.

[46] S. Bollmann *et al.*, "DeepQSM - using deep learning to solve the dipole inversion for quantitative susceptibility mapping," *Neuroimage*, vol. 195, pp. 373–383, 2019.

[47] A. Deistung, F. Schweser, and J. R. Reichenbach, "Overview of quantitative susceptibility mapping," *NMR Biomed.*, vol. 30, no. 4, 2017.

[48] Y. Wang, Y. Chen, D. T. Utriainen, and E. M. Haacke, "Automatic segmentation of deep grey matter structures for iron quantification," in *27th Annual Meeting of ISMRM*, 2019.

[49] P. C. Hansen and D. P. O'Leary, "The Use of the L-Curve in the Regularization of

Discrete Ill-Posed Problems," *SIAM J. Sci. Comput.*, vol. 14, no. 6, pp. 1487–1503, 1992.

[50] T. O. M. Goldstein and S. Osher, "The split bregman method for l1 regularized problems," *SIAM J. Imaging Sci.*, vol. 2, no. 2, pp. 323–343, 2009.

[51] W. Yin, S. Osher, D. Goldfarb, and J. Darbon, "Bregman iterative algorithms for L1-minimization with applications to compressed sensing," *SIAM J. Imaging Sci.*, vol. 1, no. 1, pp. 143–168, 2008.

[52] R. Barrett *et al.*, "Templates for the solution of linear systems: Building blocks for iterative methods," *SIAM*, 1994.

[53] S. Boyd, N. Parikh, E. Chu, B. Peleato, and J. Eckstein, "Distributed Optimization and Statistical Learning via the Alternating Direction Method of Multipliers," *Found. Trends Mach. Learn.*, vol. 3, no. 1, pp. 1–122, 2010.

[54] S. Buch, S. Liu, E. M. Haacke, and J. Neelavalli, "Simulated 3D brain model to study the phase behavior of brain structures," in *20th Annual Meeting of ISMRM*, 2012, p. 2332.

[55] S. Buch, S. Liu, Y. Ye, Y. C. N. Cheng, J. Neelavalli, and E. M. Haacke, "Susceptibility mapping of air, bone, and calcium in the head," *Magn. Reson. Med.*, vol. 73, no. 6, pp. 2185–2194, 2015.

[56] C. Lee, E. Baker, and D. Thomasson, "Normal Regional T1 and T2 Relaxation Times of the Brain at 3T," *Proc Intl Soc Magn Reson Med*, vol. 14, p. 2006, 2006.

[57] Z. Wang, A. C. Bovik, H. R. Sheikh, and E. P. Simoncelli, "Image quality assessment: From error visibility to structural similarity," *IEEE Trans. Image Process.*, vol. 13, no. 4, pp. 600–612, Apr. 2004.

[58] B. Avants, N. Tustison, and G. Song, "Advanced Normalization Tools (ANTS)," *Insight J.*, vol. 2, pp. 1–35, 2009.

[59] B. B. Avants, N. J. Tustison, G. Song, P. A. Cook, A. Klein, and C. Gee, "A Reproducible Evaluation of ANTs Similarity Metric Performance in Brain Image Registration," *Neuroimage*, vol. 54, no. 3, pp. 2033–2044, 2011.